# ROS MEDIATED THERANOSTIC MATERIALS

**Ayaulym Abilova,** BSc of Biological Sciences

**Submitted in fulfillment of the requirements**
**for the degree of Master of Science**
**in Biomedical Engineering**

NAZARBAYEV UNIVERSITY

**School of Engineering and Digital Sciences**
**Department of Chemical & Materials Engineering**
**Nazarbayev University**

53 Kabanbay Batyr Avenue,
Astana, Kazakhstan, 010000

**Supervisors:** Chang-Keun Lim
Dhawal Shah

**April 2023**

# Declaration

I hereby, declare that this manuscript, entitled “ROS mediated theranostic materials”, is the result of my own work except for quotations and citations which have been duly acknowledged.

I also declare that, to the best of my knowledge and belief, it has not been previously or concurrently submitted, in whole or in part, for any other degree or diploma at Nazarbayev University or any other national or international institution.

Name: Ayaulym Abilova

Date: 07.04.23

# Acknowledgements

I would like to express my deep gratitude to Professor Chang-Keun Lim for giving me the opportunity to work on this project and for his patient guidance, insightful feedback, unwavering encouragement, and support throughout the entire process of researching and writing this thesis.

I thank Professor Dhawal Shah for his endless support and encouragement and for always being available to provide me with feedback and guidance. Also, I want to express my appreciation to Professor Abdul Rajjaq and Dr. Bholanath Maity for their invaluable insight into DFT calculations.

I express my gratitude to Professor Tri Pham for his invaluable assistance with cell imaging; I am also grateful to Professor Timur Atabayev and Dr. Baurzhan Umbayev for their technical support.

I am also deeply grateful to Dr. Anatoly Peshkov, Dr. Yerkin Shabdan, Anel Urazaliyeva, Almaz Beisenbayev, and Samal Kaumbekova, who have supported and encouraged me along the way. I would also like to thank PMBP lab members.

Finally, I would like to express my gratitude to my family and friends for their support and patience throughout my study.

# Table of Contents

# List of Abbreviations & Symbols

| | |
|---|---|
| CL | Chemiluminescence |
| CIEEL | Chemically Initiated Electron Exchange Luminescence |
| CPPO | Bis[3,4,6-trichloro-2-(pentyloxycarbonyl)phenyl] oxalate |
| CRET | Chemiluminescence Resonance Energy Transfer |
| DCM | Dichloromethane |
| DFT | Density Functional Theory |
| DI water | Deionized water |
| DMSO | Dimethyl sulfoxide |
| DNA | Deoxyribonucleic acid |
| FL | Fluorescence |
| FOC | Fluorinated Oxalate Compound |
| FRET | Fluorescence Resonance Energy Transfer |
| MRC-5 | Medical Research Council cell strain 5 |
| MTT | (3-(4, 5-dimethylthiazolyl-2)-2, 5-diphenyltetrazolium bromide) assay |
| MRI | Magnetic Resonance Imaging |
| NPs | Nanoparticles |
| PDT | Photodynamic Therapy |
| PLGA | Poly(D,L-lactide-co-glycolide) ester terminated |
| POCL | Peroxyoxalate Chemiluminescence |
| PpIX | Protoporphyrin IX disodium salt |
| PS | Photosensitizer |
| R6G | Rhodamine 6G |
| ROS | Reactive oxygen species |
| TEM | Transmission Electron Microscope |

# List of Figures

# List of Tables

# Abstract

Image-guided therapy or theranostics is a promising emerging approach in drug delivery systems that allows for overcoming severe side effects of conventional treatment options. Reactive oxygen species (ROS) are essential players in normal cell functioning; however, their abnormal metabolism is associated with numerous acute and chronic conditions. Therefore, the overproduction of ROS may serve as an attractive biomarker for tracking the early progression of the diseases. Herein, we studied ROS activatable nanoparticles comprising peroxyoxalate esters capable of multimodal imaging and smart drug release, simultaneously, in the biomarker-rich microenvironment. A fluorinated oxalate compound (FOC), chemiexcitation source, fluorophore, or photosensitizer were co-encapsulated with Pluronic F-127 forming nanoparticles (NPs). Upon perhydrolysis reaction with hydrogen peroxide - the most stable and abundant form of ROS, oxidation of the FOC results in degradation of the hydrophobic matrix of the NPs, giving rise to the chemiluminescence (CL) emission, the release of fluorinated alcohol acting as $^{19}F$ MRI contrasting agent and drug release, at the same time. Thus, the ROS-sensitive nanoprobe may enable precise tracking of the inflamed tissues (cells undergoing excessive oxidative stress) via multiple imaging modalities accompanied with biomarker-specific drug delivery.

*Keywords:* Reactive oxygen species, peroxyoxalate chemiluminescence, $^{19}F$ NMR/MRI, drug delivery, bioimaging, theranostics

# Chapter 1 - Introduction

Current strategies for active-targeting drug delivery and cancer imaging mainly focus on incorporating certain membrane proteins or enzymes that are abundant in cancerous cells [1, 2]. However, due to the instability and individual differences of the tumor cells, the targeting efficiency may be prone to drawbacks [3]. Therefore, the development of nanoprobes responsive to the non-protein hallmarks of the tumors, such as pH, hypoxia and ROS, holds great potential [4, 5]. ROS are essential players in normal redox-dependent cell functioning; however, their abnormal metabolism may cause oxidative damage and induce inflammation. Thus, an excessive amount of high-energy oxygen bearing molecules like hydrogen peroxide may serve as an attractive biomarker for tracking the progression of the diseases [5, 6, 7]. The development of novel oxalate compounds sensitive to hydrogen peroxide may expand the theranostic (therapeutic and diagnostic) potential of peroxyoxalate chemiluminescence systems. Moreover, the reaction products such as alcohol and carbon dioxide can allow the use of multiple imaging modalities like magnetic resonance imaging (MRI) and ultrasound (US) accompanied with the site-selective drug release.

Peroxyoxalate chemiluminescence (POCL) is an indirect or sensitized type of luminescence because *in situ* generated high-energy intermediate transfers energy to the fluorophores nearby, thus light emission ranging from ultraviolet to near-infrared regions could be achieved, making it an attractive platform for various applications [8]. Overall, the mechanism behind POCL is a complex and multistep process where light-generating and side reactions may occur simultaneously [9]. POCL involves highly reactive material that can fuel the reaction like bis[2,4,5-trichloro-6-(pentyloxycarbonyl)phenyl]oxalate (CPPO). Once the oxalate compound and

hydrogen peroxide react, “key intermediate” - 1,2-dioxetanedione is formed. Then, the intermediate can transfer energy to the fluorophore nearby, followed by light emission from the excited luminophore [8,9]. Co-localization of the oxalate compounds and dye inside the nanoparticle is a promising approach allowing a high sensitivity towards ROS. This framework was employed for the development of ROS-responsive theranostic nanoplatforms (Figure 1.1). The fluorinated oxalate compound (FOC) that can act as a fuel for chemiluminescence was synthesized (Figure 1.1). Then, they assembled into the nanoparticle: due to the hydrophobic nature of the FOC molecule, they aggregated at the core of the nanoparticle along with the dye or photosensitizer drug (rubrene or protoporphyrin IX (PpIX)) while the surfactants Pluronic F-127 was used for the biocompatibility and PLGA for the stability of the nanostructure. ROS-mediated POCL reaction triggers oxidation of the peroxalate ester bond and forms a “key intermediate” and two hydrophilic fluorinated alcohol molecules. Subsequent degradation of the nanoparticles' hydrophobic matrix results in the drug's release. Thus, the products of the reaction enable activation of several imaging modalities: chemiluminescence signal emission, the liberated hydrophilic fluorinated alcohols serve to radiometrically image a $^{19}F$ MRI signal, decomposition of the intermediate to form carbon dioxide gas molecules could be investigated for the ultrasound imaging, degradation of the matrix in the biomarker-rich environment results in the site-specific drug delivery. Thus, imaging the tissues with elevated oxidative stress and delivering drugs to the same location could be realized. Hydrogen peroxide generated in inflamed tissues may be visualized as a biomarker of the progression of various inflammatory diseases. The molecular mechanisms involved in the POCL reaction were studied by the density functional theory (DFT) calculations to screen the reactivity of the fluorinated peroxalate compound with hydrogen peroxide and water.

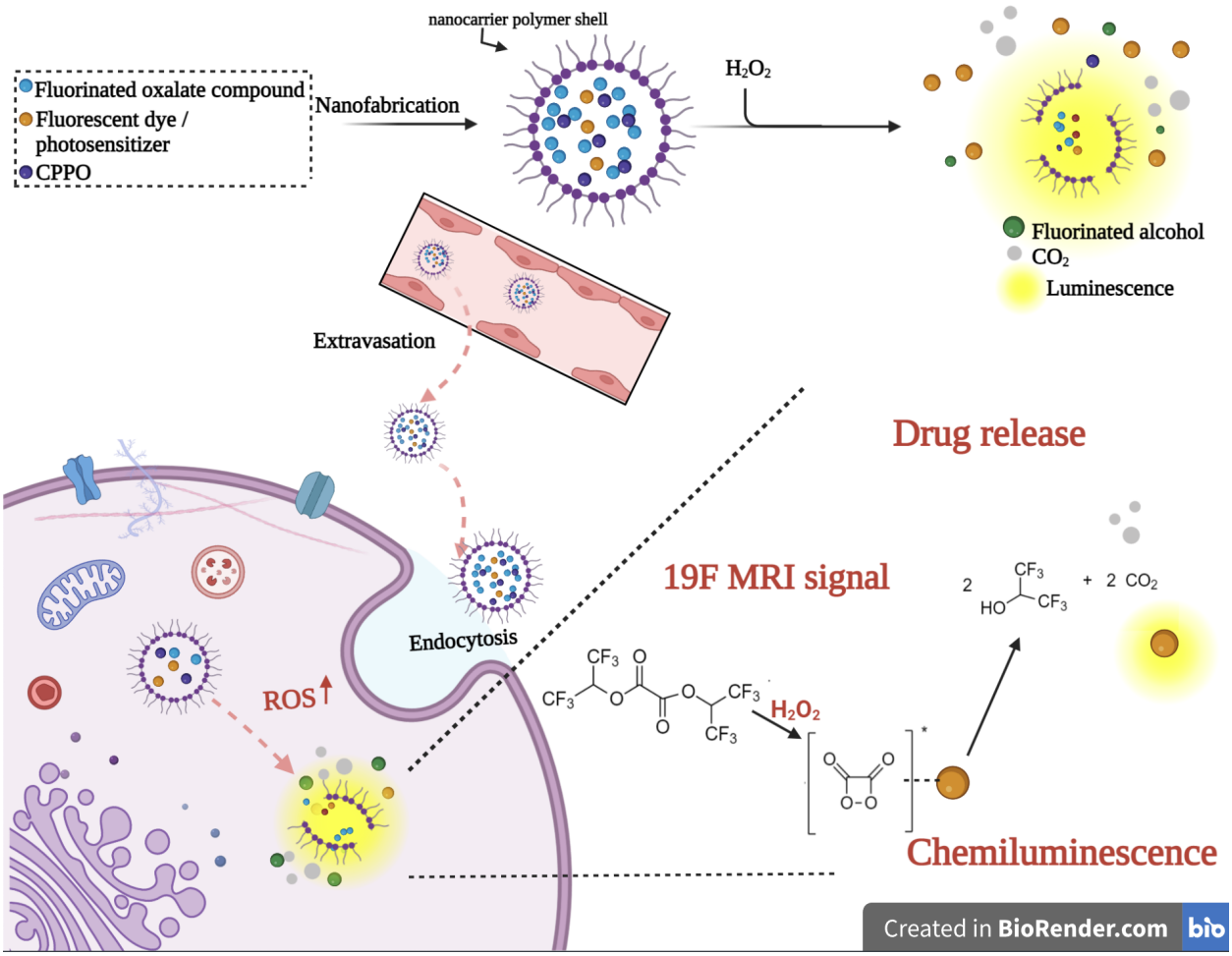


***Figure 1.1. Schematic illustration of engineering reactive oxygen species-mediated theranostic nanoparticles. The image was created using the BioRender.com website.***

**Aims and Objectives**

The aim is to develop ROS-sensitive theranostic nanocarriers that can turn on the ultrasound, $^{19}F$ magnetic resonance, and chemiluminescent imaging modalities and deliver therapeutic materials to the ROS-overexpressed site *in vivo*.

The objectives are:

1. Performing DFT calculations for the estimation of the reactivity and stability of the fluorinated oxalate compounds.
2. Synthesis of the hydrogen peroxide-sensitive fluorinated oxalate compounds.

3. Fabrication of the nanoparticles containing fluorinated oxalate compounds, fluorophores, and drugs.
4. Demonstration of theranostic nanocarriers.

# Chapter 2 - Literature Review

## 2.1 Inflammation and Reactive oxygen species

Inflammation is an integral physiological response toward injuries, pathogenic infections, ischemia-reperfusion, or chemicals. Acute inflammation is regulated by the innate immune system expressing the pattern recognition receptors involved in recognition of the pathogens entering the body. Neutrophils are first recruited to the infected tissue to promote the containment of the pathogens through phagocytosis, degranulation, and the release of reactive oxygen species (ROS) [5]. However, the excessive and uncontrolled inflammatory response can result in organ damage and be associated with pathological conditions such as acute organ injuries, sepsis, rheumatoid arthritis, cancer, and neurodegenerative disorders [7]. Understanding the persistent role of inflammations in chronic diseases has fueled the interest in developing agents for early diagnosis and suppression of the acute response.

Reactive oxygen species (ROS) is a general term for a family of species derived from molecular oxygen. ROS induces oxidative modifications in biological macromolecules by undergoing a series of reduction-oxidation reactions. The mitochondrial electron transport chain (ETS) produces superoxide ($O_2^{\cdot -}$), which is then converted to hydrogen peroxide ($H_2O_2$) via a dismutation reaction accelerated by superoxide dismutase [5, 12]. One of the most well-studied reactive oxygen species, $H_2O_2$, is continuously generated via NADPH oxidases [5,10]. Due to the

compound's stability, hydrogen peroxide remains the most abundant type of reactive oxygen species. Intracellular physiological concentrations of the $H_2O_2$ are in the nanomolar range [5]. In comparison, the levels of $O_2^{\cdot -}$ are a thousand times less and associated with more localized responses. $H_2O_2$-mediated cell signaling occurs through reversible oxidation of the thiol residue of cysteine and redox relay mechanisms [10]. The downstream effectors are involved in critical cell functions such as metabolism, transcription, and cell replication. Glutathione (GSH) peroxidase is a primary reducing cofactor of $H_2O_2$ in the mitochondrial matrix. $O_2^{\cdot -}$ was shown to affect mitochondrial activity by disrupting transition metal ion clusters (Fe-S) in the citric acid cycle releasing iron [5]. The reaction of $H_2O_2$ with iron ions results in the one-electron reduction and formation of another oxidant hydroxyl radical ($OH^-$). $OH^-$ is the most reactive biological oxidant serving as a biomarker of oxidative damage due to the non-specific reactions with important biomolecules like DNA, RNA, and lipids [5]. At low levels, oxidative stress is essential for physiological redox signaling. However, excessive oxidant concentration may promote reactions with unspecific targets and aberrant signaling pathways. The interactomes of ROS are summarized in Figure 2.1.1. It was suggested that $H_2O_2$ contents in tumors might be up to 100 times higher than in normal tissues due to the abnormal metabolism of the cancer cells in cancerous tissues [6,7]. Therefore, $H_2O_2$ remains an attractive target for the novel environment-responsive drug delivery and visualization (theranostic) systems in various disease models.

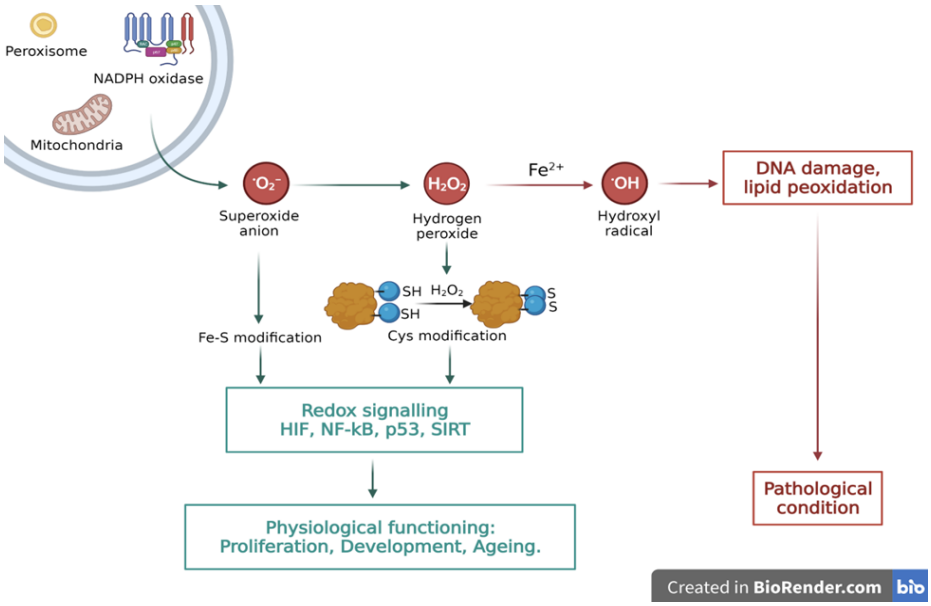


***Figure 2.1.1. Reactive oxygen species (ROS) interactome. Based on [5]. The figure was created on the BioRender.com website.***

Rapid development in biomedical imaging has enabled early diagnosis of disease progression, intraoperative image-guided surgery, and precision therapy [11]. Optical imaging employs properties of the photons: when added to the biological environment, the emission of exogenous optical probes allows visualization of the tissues, microstructures, or microenvironments [13]. High sensitivity, spatiotemporal resolution, and fast response allowed applications for non-invasive, real-time visualization of biological tissues. The optical imaging probes for sensing and imaging are based on fluorescence, bioluminescence, and chemiluminescence [11, 14, 8]. Fluorescence imaging requires external excitation light. Moreover, the issues with the light penetration depth and autofluorescence of the endogenous tissues complicate the visualization process [8]. Bioluminescence relies on enzymatic catalysis and may require genetic modifications for additional conjugation of the targeting molecules enabling enhanced selectivity [14]. Chemiluminescence, in contrast, holds the potential for visualization in

biological systems because of the ease of implementation [8,12]. In chemiluminescence, light emission arises from the chemical reaction involving energy transfer in the presence of initiators like $H_2O_2$ and $O_2^{\cdot -}$. External light-free design of the chemiluminescent imaging and the following absence of autofluorescence level led to improved *in vivo* imaging capability.

The energy states are quantized and contain different vibrational levels. Chemiluminescence occurs when an electronically excited state product returns to the ground state depicted as S0 in Figure 2.1.2. Overall, it could be noted that emissions of fluorescence and chemiluminescence are the same, however, the excitation processes are different: absorption of ultraviolet or visible light and chemical reaction, respectively. Chemiluminescence is described as a dark-field technique because of the absence of the background level signal [8]. This is advantageous for eliminating the background autofluorescence and reaching a lower limit of detection.

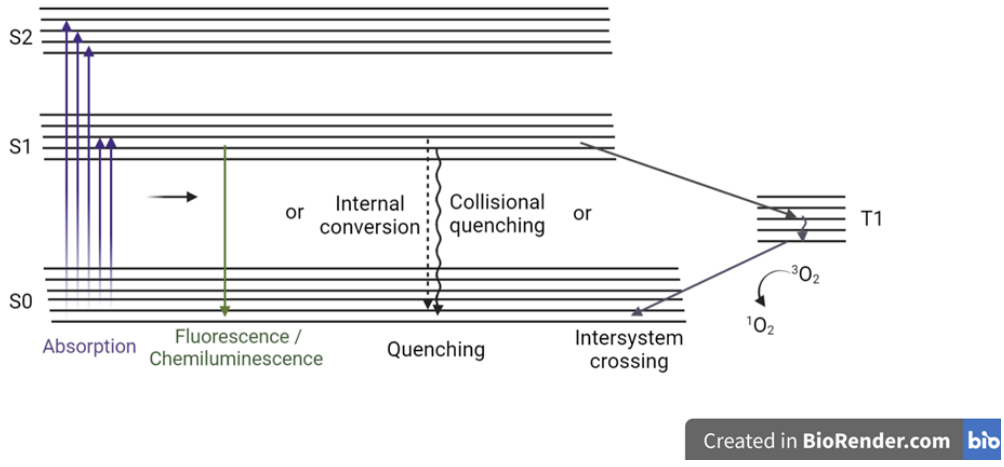


***Figure 2.1.2. Jablonski diagram. Based on [8]. The figure was created in BioRender.com website.***

The quantum mechanical processes enable the spectral properties of the probes. However, there are a number of obstacles: emission intensity, short emission wavelength, and luminescence lifetime [8]. Herein, chemiluminescent probes based on different functional groups used for the molecular imaging of the reactive oxygen species and visualization of the inflamed tissues were summarized.

### 2.2. Optical probe design optimizations

#### 2.2.1 Chemiluminescent properties considerations

The chemiluminescent properties of optical probes depend on the fluorescent dyes' stability, quantum yield, and other factors like the reaction temperature presence of the catalyst. Higher signal intensity is achieved when a fluorescent dye with a high quantum yield is used. Also, the concentration of the dye is an essential factor. Although chemiluminescence efficiency is weaker when the dye concentration is low, a high concentration of the dye may result in fluorescence concentration quenching due to aggregation [8, 15, 17].

For peroxyoxalate chemiluminescence, basic conditions were shown to catalyze the reaction. Moreover, increasing the temperature is expected to increase the collision frequency, but quenching at higher temperatures also occurs. The solvent may also impact chemiluminescence based on the antenna effect [18].

#### 2.2.2 Specificity considerations

The reactive oxygen species specificity of the probes is achieved via the incorporation of modifiable groups or ROS-sensitive moieties to achieve better targeting [12]. The most frequently

reported modification sensitive to hydrogen peroxide is incorporating a biomarker-cleavable arylboronic ester group [8].

The biodistribution of optical probes is one of the most challenging obstacles. Despite a moderate accumulation of the optical probes in the tumor site, non-desired accumulation in the liver or lungs occurs frequently. Such accumulation depends on various factors such as the size of the nanoparticles, rigidity, surface charge, etc. Coating with amphiphilic polymers like PEG, DSPE-PEG was commonly used for enhanced biocompatibility of the nanoreporters [18-21].

Another important pharmacokinetic property for estimating the clinical translation of optical theranostic agents is the pathway of clearance. Nanoparticles resistant to biodegradation may accumulate in the body and induce toxicity [13]. Hepatobiliary clearance refers to the metabolism and degradation of the nanoparticles that occurs by macrophages through phagocyte systems in the liver and spleen, followed by excretion through the bile duct. While in kidney clearance, nanoparticles are filtered in glomerular filtration and minimally metabolized, thus, minimizing potential side effects [14].

### 2.3. Promising particle-based theranostic platforms.

#### 2.3.1 Schaap's dioxetane-based systems

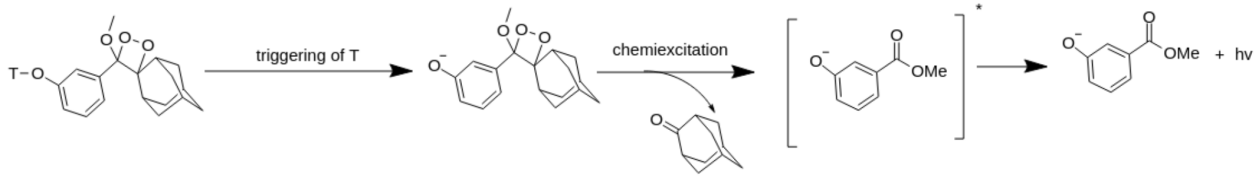


Note: T is targeting moiety

***Figure 2.3.1.1. Schematic illustration of Schaap's dioxetane-based systems. The figure was created in ChemDraw software.***

Schaap's dioxetane-based chemiluminescent probes' sensitivity toward the analytes is achieved by incorporating the sensing moiety. Once the sensing moiety or protecting group is removed in the presence of the analyte, the phenolate group generates emission at the wavelength of 470nm [13]. For *in vivo* applications, the systems based on Schaap's dioxetane undergo modifications which include: (1) chemiluminescence resonance energy transfer (CRET) and/or fluorescence resonance energy transfer (FRET) processes to another fluorophore; (2) conjugation with the electron-withdrawing groups [18].

Huang et al. have created a dual-channel probe $MRP_D$ for the simultaneous visualization of the clearance and acute kidney injury via chemiluminescence in response to $O_2^{\cdot-}$ [19]. Because of the minimized tissue autofluorescence in the chemiluminescence imaging, sensitive visualization of the upregulated $O_2^{\cdot-}$ was achieved, enabling early detection of the acute kidney injury before it affected the glomerular filtration rate [14, 18]. Thus, reportedly outperforming the other real-time imaging methods for at least 36 hours. The probe was based on Schaap's dioxetane with biomarker-cleavable trifluoromethanesulfonate in the phenol group. The intermediate phenolate dioxetane underwent a chemically initiated electron exchange luminescence process resulting in 3000-fold chemiluminescent signal enhancement [19].

The study by Cui et al. has demonstrated the efficacy of the $O_2^{\cdot-}$ activatable nanoreporters incorporating semiconducting polymers (SPNR) [20]. The design of the nanoreporters included semiconducting polymer and Schaap's dioxetane containing trifluoromethanesulfonate for biomarker specificity. SPNRs are intrinsically fluorescent, however, chemiluminescence was observed only upon activation by $O_2^{\cdot-}$. Due to the efficient resonance energy transfer, SPNR could selectively turn on the chemiluminescence signal at 700 nm, exhibiting 490-fold signal

enhancement. A low limit of detection promoted using nanoprobe for real-time *in vivo* imaging of cancer immunotherapy [20].

Schaap's dioxetane-based systems were also employed to monitor cerebral ischemia-reperfusion injury-induced $H_2O_2$ fluxes and arsenic trioxide-induced leukemia. Ye et al. proposed an $H_2O_2$-CL-510 small-molecule chemiluminescent probe sensitive to $H_2O_2$, generating strong chemiluminescent emission without any external excitation [21]. The design was based on the masked phenoxy-dioxetane platform with salicylaldehyde sensing moiety that is selectively cleaved to expose phenoxy-dioxetane undergoing chemiexcitation. 430-fold enhancement of chemiluminescence was observed after the reaction with $H_2O_2$. The system's efficacy was shown via chemiluminescent imaging *in vitro* and real-time monitoring of rat brains [21].

### 2.3.2 Donor - acceptor - donor structures

Integrating the two electronic donors (D) at both sides of the electronic acceptor enables extending fluorophore's emission. The main obstacles associated with such conjugation included poor water solubility and aggregation-induced fluorescence quenching.

Chen et al. proposed NIR-II fluorophore based on benzothiadiazole-core with two tetraphenylene groups acting as hydrophobic molecular rotors and two $H_2O_2$-sensitive nitrophenyloxoacetamide units at both ends of the core for recognition and fluorescence quenching [22]. The BTPE-$NO_2$ was then encapsulated to Pluronic F127 for enhanced biocompatibility. Moreover, the probe enabled multispectral optoacoustic tomography (MSOT) imaging for visualizing and locating the disease foci.

Sun et al. reported the NIR-II excitation phototheranostic platform for synergistic photothermal therapy, chemo, and chemodynamic therapies of bone cancer metastasis [23]. The

platform was based on dopamine-modified donor-acceptor-donor small molecules serving as a photoactive agent and drug carrier. In an acidic and $H_2O_2$-abundant tumor microenvironment, the boronate-catechol linkage was cleaved, and bortezomib chemotherapeutic drug and $Fe^{2+}$ ions triggering chemodynamic therapy were released [23]. Moreover, the nanoplatform exhibited bone targeting ability, and significant accumulation in breast cancer bone metastases was shown.

### 2.3.3 Peroxyoxalate-based systems

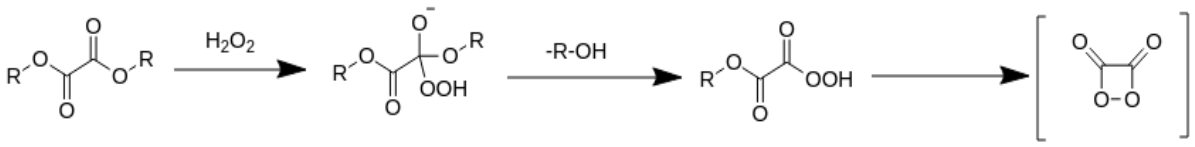


***Figure 2.3.3.1. Schematic illustration of peroxyoxalate-based systems. The figure was created in ChemDraw software.***

Among the variety of chemiluminescent probes, $H_2O_2$ -sensitive and selective peroxyoxalate chemiluminescence (POCL) was implemented frequently to visualize endogenous inflammations. The observed luminescent signal of chemiluminescence is “fueled” by the chemical reaction (Figure 2.3.3.1). The reaction of POCL proceeds via the formation of high-energy intermediate 1,2-dioxetanedione, followed by energy transfer and excitation of the adjacent fluorophore [8, 17]. Bis[2,4,5-trichloro-6(pentyloxycarbonyl)phenyl] oxalate - CPPO was a commonly used compound for the biological application of POCL. The development of novel oxalate compounds may expand the theranostic potential of POCL, thereby allowing the use of multiple imaging modalities like magnetic resonance imaging (MRI) and ultrasound (US).

Yan et al. reported the synthesis of wavelength-tunable nanoparticles based on vitamin E (safe antioxidant) conjugated with the peroxalate ester and encapsulating different fluorophores to

generate the chemiluminescence signal [24]. Once reacted with $H_2O_2$, OVE's high-energy and unstable intermediate was expected to excite different fluorescent probes. The emission wavelength varied from blue to NIR light depending on the loaded fluorophore. Derived nanoprobes were then used to visualize diseases like peritonitis, acute liver and lung injury, and tumors.

Jeon et al. proposed a system based on a peroxalate ester bond containing dibutyl oxalate also acting as a chemiluminescence donor and verteporfin acting as a sonosensitizer and CL acceptor assembled into a PEG shell [25]. It was suggested that peroxalate/ photosensitizer-based CRET-NPs could be long-acting cancer phototheranostic agents: allowing effective photoacoustic imaging (PA) and photodynamic therapy (PDT). PA signal enhancement was achieved via thermal expansion-induced vaporization, while ROS quantum yield enhancement was through photochemical reactions.

In their other study, Jeon et al. used a similar setup for a CRET-based immunostimulatory nanoparticles (iCRET NPs). Membrane rupture and thus immunogenic cell death in the tumor microenvironment (TME) was achieved via sonoimmunotherapy where generated carbon dioxide ($CO_2$) bubbles ruptured the cancer cell membrane in the presence of US [26]. iCRET NPs effectively improved the ROS quantum yields of the sonosensitizer. $CO_2$-mediated immunogenic cell death and efficient anticancer were proved on 4T1 tumor-bearing mice.

Ding et al. suggested synergistic trimodal cancer therapy by loading CPPO, chlorine e6 (Ce6), and doxorubicin (Dox) prodrug Dox-EMCH into M1 macrophage-derived extracellular vesicle [27]. Active targeting of tumors was achieved via the native tumor-homing capability of the M1CCD vesicles. The reaction between hydrogen peroxide and CPPO generated chemical

energy that activated Ce6, giving rise to chemiluminescence signal for imaging and singlet oxygen for photodynamic therapy (PDT). The membrane rupture caused by excessive singlet oxygen led to the release of Dox-EMCH, which was activated in the tumor microenvironment and penetrated the deep hypoxic areas. Thus, immunotherapy, PDT, and chemotherapy worked in an intersynergistic manner, resulting in potent anticancer efficacy with minor side effects.

Chen et al. [28] created the all-in-one nanohybrid mSCCC@SA nanoparticles readily constructed using mesoporous silica as a template loaded with $CaO_2$. PDT reaction was fueled by a high-energy intermediate 1,2-dioxetanedione formed from the chemiluminescent agent (CPPO). CPPO and photosensitizer (Ce6) were co-encapsulated into the porous silica cavity. The steric acid surface coating was used to prevent early release. This design provided a self-supply of $H_2O_2$ and $O_2$ for external light-free PDT and calcium-overloaded therapy in orthotopic tumors.

Ratiometric chemiluminescence/fluorescence reporters were also studied for the visualization and ratiometric monitoring of the hydroxyl radical. Wu et al. [29] suggested using diene electrochromic material (1-Br-Et) fluorescent and photoacoustic (FL/PA) bimodal probes. 1-NP-FA displayed large FL780/FL1113 (~1026-fold) and PA755/PA905 (~22-fold) turn-on ratios in response to hydroxyl radical, thereby ensuring high sensitivity for the detection and improved spatio-temporal resolution.

Su et al. proposed 2SeFT-PEG/Ce6 micelles with $^1O_2$-activated ratiometric NIR-II CL/FL. The system was based on the thiophene-based small molecule and photosensitizer Ce6 micelles for real-time monitoring of PDT efficacy [30]. Once exposed to $^1O_2$ reduction, oxidation reactions improved chemiluminescence (CL) and diminished fluorescence (FL) signals. The platform's

efficacy was evaluated based on the mice tumor model for guiding and real-time evaluation of the PDT effect.

**Table 2.3.1. Properties and applications of optical probes.**

| | Optical probe | Additional imaging modality //treatment method | Disease model | ROS biomarker | ROS-sensitive linker | Emission wavelength (nm) | LOD (nM) | Ref |
|---|---|---|---|---|---|---|---|---|
| Schaap's dioxetane based | | | | | | | | |
| 1 | $MRP_D$ | FL (dual-channel) | AKI | $O_2^{\cdot -}$ | $CF_3SO_3$ | 540 | 13 | [19] |
| 2 | SPNR | FL | T | $O_2^{\cdot -}$ | $CF_3SO_3$ | 700 | 0.118 | [20] |
| 3 | H2O2-CL-510 | FL | C I/R | $H_2O_2$ | salicylaldehyde | 510 | calc. 7.1 | [21] |
| Donor-acceptor-donor based | | | | | | | | |
| 4 | BTPE-NO2 | optoacoustic tomography | IC, LI, I/RI | $H_2O_2$ | nitrophenyloxoacetamide | 950 | 740 | [22] |
| 5 | BTZ/Fe2+@BTF/ALD | FL PTT/chemotherapy/CDT | BM | $H_2O_2$ | boronate | 1124 | - | [23] |
| Peroxyoxalate based | | | | | | | | |
| 6 | OVE | - | AKI, LI, P, T | $H_2O_2$ | - | 432 - 855 | - | [24] |

| | | | | | | | | |
|---|---|---|---|---|---|---|---|---|
| 7 | CRET-NP (Ce6) | PA, PDT | T | $H_2O_2$ | - | 670 | - | [25] |
| 8 | iCRET | SDT | T | $H_2O_2$ | - | 633 | | [26] |
| 9 | M1CCD | PDT | T | $H_2O_2$ | - | | - | [27] |
| 10 | mSCCC@ SA NPs | PDT, calcium overloaded therapy | T | $H_2O_2$ | - | | - | [28] |

AKI: acute kidney injury; IC: interstitial cystitis; LI: liver injury; I/RI: ischemia-reperfusion injury, P: peritonitis, T: tumor; C I/R: cerebral ischemia-reperfusion; FL: fluorescence, SDT: sonodynamic therapy, PA: photoacoustic; $CF_3SO_3$: trifluoromethanesulfonate.

### 2.4. Summary and Perspectives

In contrast to the other available fluorescence sensing and imaging techniques, chemiluminescence has a series of advantages allowing it to build an efficient system for tracking the progression of inflammatory diseases and molecular imaging of the reactive oxygen species. The systems are enhanced with the CRET and FRET processes.

### 2.5 DFT calculations

Nowadays, computational chemistry has opened new avenues for studying the structures and properties of molecules. Quantum chemical calculations that became possible due to the substantial progress in computational methods and computational power have provided new mechanistic insights into organic chemistry, allowing a deeper understanding of chemical reactivities and selectivity [31].

Insufficient stability of the compounds may cause several complications for *in vivo* applications. Because hydrolysis (reaction with water) and perhydrolysis (reaction with hydrogen peroxide) may coincide in biological systems, optimization of chemical structures for peroxalate compounds *in silico* using density functional theory (DFT) calculations were attempted.

DFT is a computational quantum mechanical modeling method used materials science to investigate the electronic structure of atoms and molecules in many-body systems. In many-body electronic structure calculation, the nuclei of the molecules are considered as fixed due to three orders of magnitude mass difference based on the Born-Oppenheimer approximation [32]. The formula gives a many-electron time-independent Schrödinger equation:

$$\hat{H}\Psi = \hat{E}\Psi = [T + U + V]\ \Psi$$

where $\hat{H}$ is the Hamiltonian, $\hat{E}$ is the total energy, T is the kinetic energy, V is the potential energy, U is the electron-electron interaction energy.

Computational chemistry software packages are commonly used to carry out DFT calculations. Gaussian is a software package developed by scientists at Carnegie Mellon University in the 1970s [33]. Calculations in Gaussian software involve using the hybrid functionals - a class of approximations to the exchange-correlation energy functional. One of the most commonly used versions Becke, 3-parameter, Lee-Yang-Parr (B3LYP) was used in the calculations.

# Chapter 3 - Experimental section

### 3.1 Materials

1,1,1,3,3,3-Hexafluoro-2-propanol and oxalyl chloride were purchased from Sigma-Aldrich Co. (St. Louis, MO, USA), diethyl ether anhydrous (Sigma-Aldrich Co.), triethylamine

anhydrous (Sigma-Aldrich Co.), Pluronic F-127 (Sigma-Aldrich Co.), Poly(D,L-lactide-co-glycolide) ester terminated (Mw 50,000-75,000) (Sigma-Aldrich Co.), deionized water, bis[3,4,6-trichloro-2-(pentyloxycarbonyl)phenyl] oxalate (TCI), Rubrene (sublimed grade) (Sigma-Aldrich Co.), Rhodamine 6G (BioChemika), Dichloromethane anhydrous (Sigma-Aldrich Co.), hydrogen peroxide (Sigma-Aldrich Co.), 3-[4,5-Dimethylthiazol-2-yl]-2,5-diphenyltetrazolium bromide (Sigma-Aldrich Co.), Protoporphyrin IX (PpIX) disodium salt (Sigma-Aldrich Co.).

### 3.2 Synthesis of Fluorinated Oxalate Compound

A hydrogen peroxide-responsive peroxalate compound bis(1,1,1,3,3,3-hexafluoropropan-2-yl) oxalate (defined as FOC) was synthesized using the following procedure. Oxalyl chloride (1.75 ml, 20.00 mmol) was put into the Schlenk tube and placed into the ice bath. Anhydrous ether (40 mL) was added to the tube under nitrogen flow. 1,1,1,3,3,3-Hexafluoro-2-propanol (4.50 mL, 42.8 mmol) was added to the tube. The mixture of anhydrous ether solution (10 mL) and triethylamine (5.5 mL, 40.15 mmol) was added dropwise. A heavy white precipitate was formed, and the solution was left to stir overnight, allowing the ice to melt. The solution was filtered using a Büchner funnel and transferred to the tube. The solution was put to the rotavapor for 650 mbar rotating at 41 $^{o}$C for 7 min to remove the bulk of the ether. The filtrate was then distilled, and the product fraction was collected at 126-127 ℃ to afford 2.386 g of a clear oil. $^{1}$H NMR, $^{13}$C NMR spectra, and $^{19}$F NMR spectra were acquired on a JNM-ECA series FT NMR spectrometer operating at 500 MHz.

### 3.3 Preparation of the Nanoparticles

FOC-CPPO nanoparticles were prepared by an emulsion solvent evaporation method, 2 mg FOC, 2 mg CPPO, 0.04 mg Rubrene, 0.4 mg PLGA was dissolved in 500 μL of dichloromethane. 2 ml of deionized water containing 40mg of Pluronic F-127 was slowly added

with sonication time of 2 min (amplitude 50%, 3s on and 1s off). Dichloromethane was evaporated in rotavapor at room temperature.

### 3.4 Characterization of Nanoparticles

Hydrodynamic size distribution and surface charge (ζ-potential) of the nanoparticles were obtained by dynamic light scattering (DLS) method using Microtrac Nanotrac Wave II (temp=24.2 ℃, ±0.1 ℃). Transmission electron microscopy (TEM) images were taken JEOL JEM−1400Plus Electron Microscope operated at 120 kV. TEM samples were prepared by dropping the sample onto the grid and excess solvent was blotted with filter paper. Negative staining was performed using 1% phosphotungstic acid.

### 3.5 Chemiluminescence and Fluorescence Measurements

Chemiluminescence and fluorescence measurements were carried out on FLS1000 Edinburgh instruments. 1 ml of 1 M hydrogen peroxide was added to 1 ml of FOC-CPPO nanoparticles sample and chemiluminescence spectra were recorded immediately and repeatedly after 1- or 1.5-min time interval. For the measurement of the fluorescence spectra, 10 μM solution of the dye in the solvent (DCM) was prepared.

In addition, the luminescence of FOC-CPPO nanoparticles at various concentrations of the hydrogen peroxide was detected using In Vivo Imaging System IVIS Spectrum CT. 270 μL of FOC-CPPO nanoparticles were mixed with 0.1 μM and 10 μM hydrogen peroxide concentrations in 96-well plates. The plate was immediately put into the imaging system to acquire luminescent signals, with an exposure time of 5 min, f/stop = 1, binning =8, optical filter for 560 nm.

### 3.6 *In vitro* Cytotoxicity Test

MTT assay to check the material toxicity was carried out with the MRC-5 human fetal lung fibroblasts cell line. The 96-well plate was seeded with the 5000 cells in each well and incubated

overnight at 37 °C in a humidified atmosphere with 5% of $CO_2$. 4 different concentrations of the FOC-CPPO nanoparticles were added. After 24 hours of incubation, 10 µL of MTT reagent was added to each well. MTT reagent was prepared by dissolving 3-[4,5-Dimethylthiazol-2-yl]-2,5-diphenyltetrazolium bromide in complete media in the concentration 5 mg/ml. Then, the solution was filtered using a 0.4 µm filter. After 4 hours, media containing MTT reagent in the wells was discarded, and 100 µl of DMSO was added to each well. Absorbance data were collected using Varioskan LUX Multimode microplate reader (at 570 nm and 630 nm for the background). The cell seeding scheme is provided below.

**Table 3.6.1. Cell seeding layout for the *in vitro* cytotoxicity test.**

| | 1 | 2 | 3 | 4 | 5 | 6 | 7 | 8 | 9 | 10 | 11 | 12 |
|---|---|---|---|---|---|---|---|---|---|---|---|---|
| A | W | 0k | 2.5k | 5k | 7.5k | 10k | 0k | 2.5k | 5k | 7.5k | 10k | W |
| B | W | 0k | 2.5k | 5k | 7.5k | 10k | 0k | 2.5k | 5k | 7.5k | 10k | W |
| C | W | C+M | C+M | C+M | C+M | C+M | C+M +W | C+M +W | C+M +W | C+M +W | C+M +W | W |
| D | W | C1: 44.4 | C1: 44.4 | C1: 44.4 | C1: 44.4 | C1: 44.4 | C1: 44.4 | C1: 44.4 | C1: 44.4 | C1: 44.4 | C1: 44.4 | W |
| E | W | C2: 22.2 | C2: 22.2 | C2: 22.2 | C2: 22.2 | C2: 22.2 | C2: 22.2 | C2: 22.2 | C2: 22.2 | C2: 22.2 | C2: 22.2 | W |
| F | W | C3: 11.1 | C3: 11.1 | C3: 11.1 | C3: 11.1 | C3: 11.1 | C3: 11.1 | C3: 11.1 | C3: 11.1 | C3: 11.1 | C3: 11.1 | W |
| G | W | C4: 5.55 | C4: 5.55 | C4: 5.55 | C4: 5.55 | C4: 5.55 | C4: 5.55 | C4: 5.55 | C4: 5.55 | C4: 5.55 | C4: 5.55 | W |
| H | W | C+M +DMSO | C+M +DMSO | C+M +DMSO | C+M +DMSO | C+M +DMSO | M | M | M | M | M | W |

**Note: The rows indicated in yellow contain standard curve data. "C": 5000 cells MRC-5 cell line, "M": media, "W": water. Concentrations (C) provided in mg/ml. Two rows are dedicated to water to maintain humidity and avoid excessive evaporation of the media.**

### 3.7 *In vitro* drug release experiments

MRC-5 cells were seeded on 8 well ibidi plates (5000 cells for each well) and incubated overnight at 37 °C in a humidified atmosphere with 5% of $CO_2$. Then, media was aspirated, and 20 µL of FOC-CPPO nanoparticles containing 2.5 mg PpIX was added to each well at different times (24 hours, 12 hours, 9 hours, 6 hours, 3 hours, 0.5 hours). For the hypoxic conditions, the plates were incubated in the anaerobic bag. Before the imaging, the media containing the sample was aspirated, and wells were washed twice with DMEM. Imaging was performed with Leica Thunder Imager and Steadycon Microscope.

### 3.8 Data analysis

The data are expressed as a mean ± standard deviation. Statistical analysis was performed using ANOVA test. Statistical comparison of the 2 groups was made by student t-test. In all cases, statistical significance was assessed at $p<0.05$. Fluorescence and chemiluminescence intensities were quantified using region of interest (ROI) analysis.

### 3.9 DFT calculations

All theoretical computations were done by using the Gaussian 16 software package and Gauss-view visualization program. DFT calculations were conducted with a hybrid functional B3LYP at 6-31G(d,p) or Def2DVP. First, the geometry optimizations of all the compounds were performed. Single-point energies were calculated using the B3LYP/6-31G(d,p). The calculations were carried out on the gas-phase optimized geometry.

### 3.9.1. 3D visualization of ESP-mapped electron density surface

Mapping of the surface was performed by generation of the electron density cubes in GausView 6.0.16 software B3LYP/6-31G basis set. First, mapping of the self-consistent field (SCF) electron density surface was done, followed by the generation of the density differences.

### 3.9.2. Locating transition states

All the transition states were optimized using the default algorithm implemented in the Gaussian 16 code. opt=(ts, noeigentest, readfc) was used for optimization at the saddle point. Moderedundant option was used to optimize the structure with the constraints specified after geometry specification. Potential energy scans and relaxed scans were set up.

# Chapter 4 - Results and discussion

## 4.1 DFT calculations results

First, the geometries of the FOC and CPPO were optimized, as shown in Table 4.1. To study the FOC behavior, the charge distribution over the surface-electrostatic potential surface has been simulated. The potential energy ($E_p$) has been calculated considering the interaction of the nuclei with electron density and imaginary positive charge (Q) following the formula $E_p=Q\varphi$, where $\varphi$ is electric potential. Electron rich regions have negative potential and were represented in red color while electron poor regions exhibited positive potential.

**Table 4.1. Geometry optimizations and 3D visualization of molecular electrostatic potential maps.**

| Name | Optimized geometry | Molecular electrostatic potential maps   | Molecular electrostatic |
|---|---|---|---|

| | | | potential surface map value on carbon atoms of the carbonyl group |
|---|---|---|---|
| FOC | 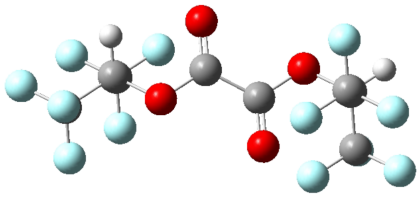 | 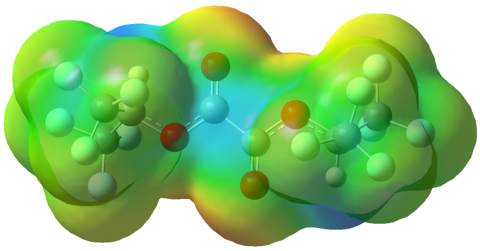 | C11: 0.046563<br>C12: 0.0465519 |
| CPPO | 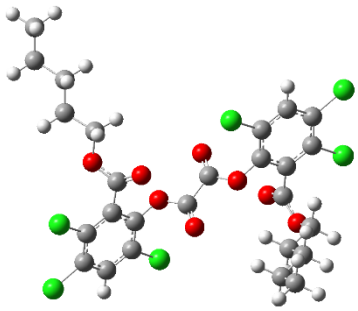 | 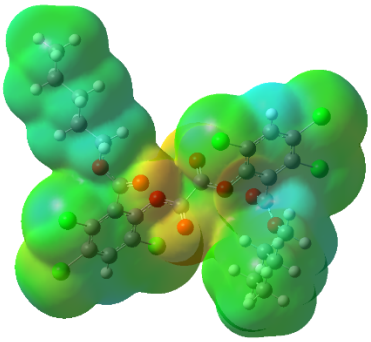 | C19: 0.00283382<br>C20:0.00188169 |

Fluorine is a highly electronegative atom; therefore, fluorinated regions exhibit electron excess. Oxygens forming peroxalate ester bonds also form a pronounced electron rich region due to the lone pairs of the electrons. Thus, exposing the electron-deficient carbocation of peroxalate ester bond and enabling nucleophilic attack by electron-rich oxygen of hydrogen peroxide. Chlorine which can be found in CPPO has some electronegativity. However, still, it could be seen that in the studied FOC compounds, carbonyl carbons are ten times more exposed. Therefore, it could be suggested that the FOC is more susceptible to nucleophilic attack.

The reaction of the FOC with hydrogen peroxide and water was studied based on the mechanism of the POCL: nucleophilic attack by the electron-rich oxygen of hydrogen peroxide to the carbonyl carbon of the FOC, followed by the formation of the high energy intermediate

(HEI) that decomposes to the carbon dioxide molecules. The transition states (TS) were optimized and checked for imaginary frequencies. Overall, it was calculated that the reaction of the FOC with hydrogen peroxide is more probable, and the products of the reaction are more stable than the reaction with water (Figure 4.1). However, calculated activation energies for perhydrolysis and hydrolysis reactions were comparable (39.8 and 37 kcal/mol, respectively) (Figure 4.1). While for CPPO the activation energy for the perhydrolysis reaction was three times less than the activation energy for the hydrolysis reaction (4.24 and 12.07 kcal/mol, respectively). These results could explain the stability of CPPO in aqueous solutions.

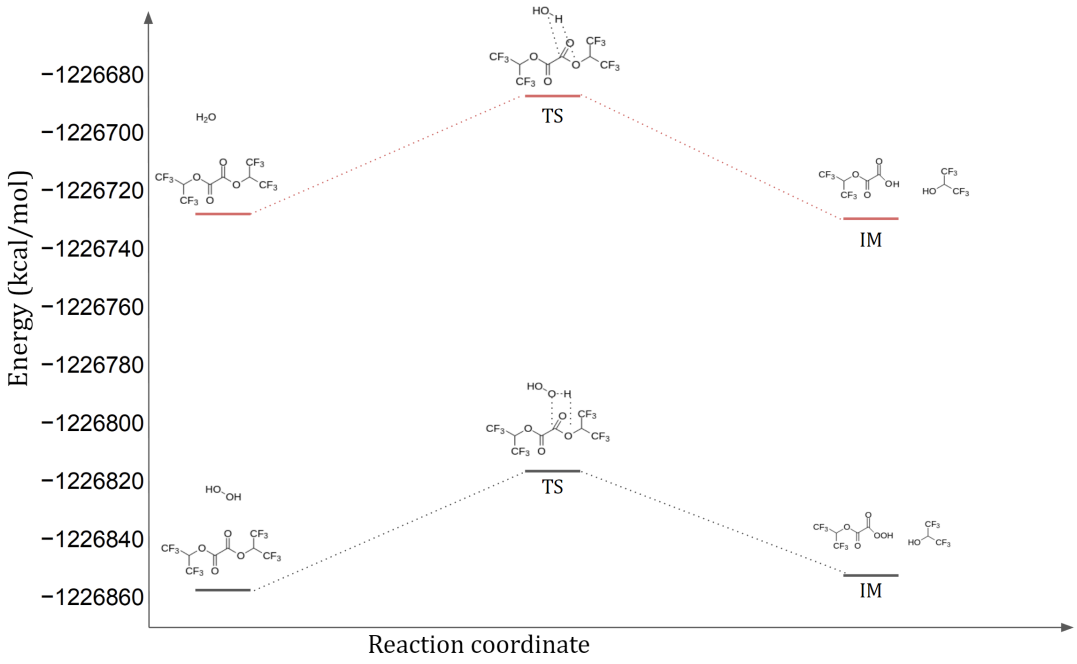


***Figure 4.1.1. Comparison of the perhydrolysis (black) and hydrolysis (red) reaction pathways of FOC with hydrogen peroxide and water, respectively.***

Then, POCL pathways for FOC and CPPO molecules were compared. It was found that CPPO, its transition states, and intermediates are significantly more stable than FOC (Figure 4.2). Moreover, the activation energy for the reaction of hydrogen peroxide with FOC was higher than

the activation energy with CPPO. These results suggest higher quantum yield for the chemiluminescence reaction for CPPO resulting from more high-energy intermediates being formed. All the optimized geometries and energies were summarized in Appendices.

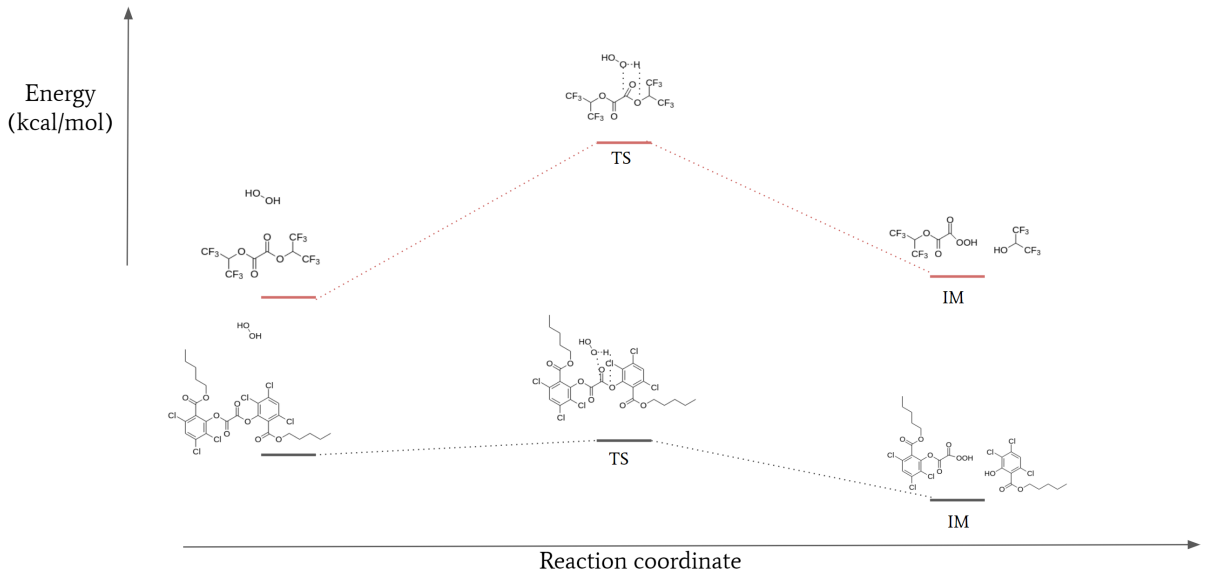


***Figure 4.1.2. Comparison of the perhydrolysis reaction pathways of FOC (red) and CPPO (black) with hydrogen peroxide.***

### 4.2 Synthesis of Fluorinated Peroxalate Compound

A novel fluorinated oxalate compound, responsive to hydrogen peroxide, was synthesized through a one-step reaction of 1,1,1,3,3,3-hexafluoro-2-propanol with oxalyl chloride, as shown in the reaction below (Figure 4.2.1).

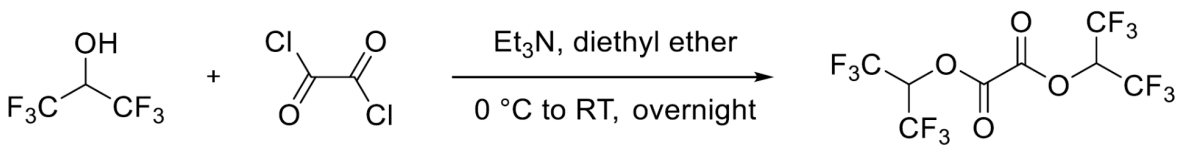


***Figure 4.2.1. Synthesis scheme of 1,1,1,3,3,3-hexafluoro-2-propanol.***

The final product, bis(1,1,1,3,3,3-hexafluoropropan-2-yl) oxalate (referred to as FOC), was structurally characterized using $^{1}H$ NMR, $^{13}C$ NMR, and $^{19}F$ NMR spectroscopy. The obtained NMR spectra confirmed the successful synthesis of FOC. Specifically, the $^{1}H$ NMR ($CDCl_3$) showed a heptet at δ 5.81, the $^{13}C$ NMR ($CDCl_3$) displayed a singlet at δ 152.35, a quartet at δ 120, and a quintet at δ 68.9, while the $^{19}F$ NMR ($CDCl_3$) exhibited a singlet at δ -72.90 (Figure 4.2.2).

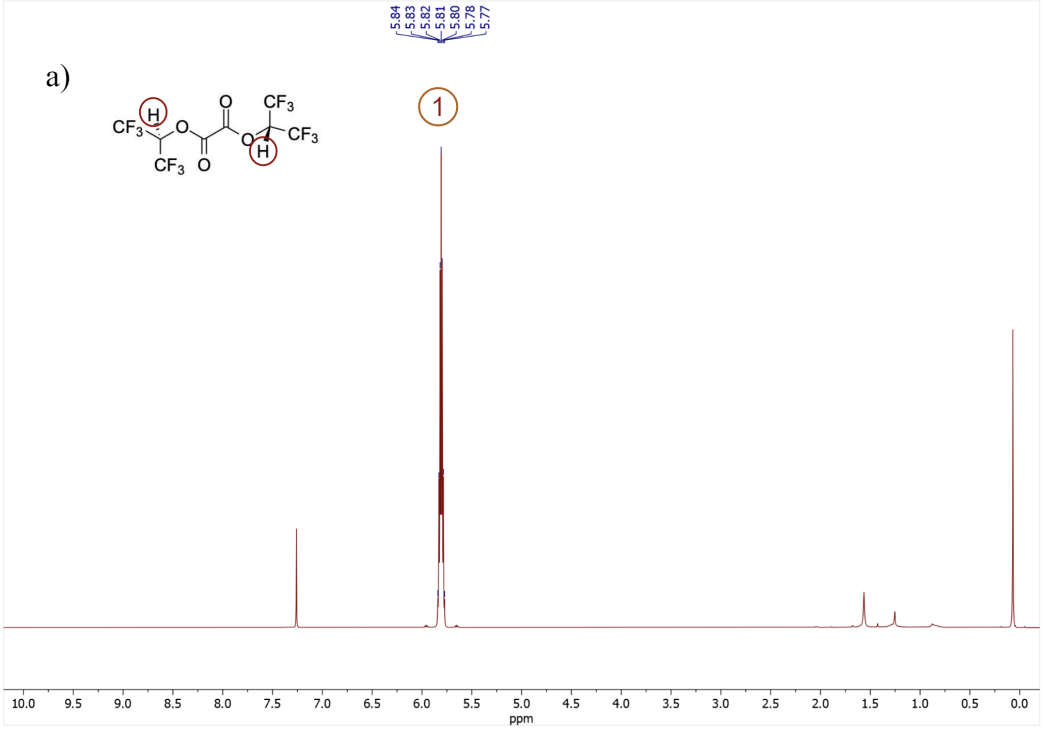

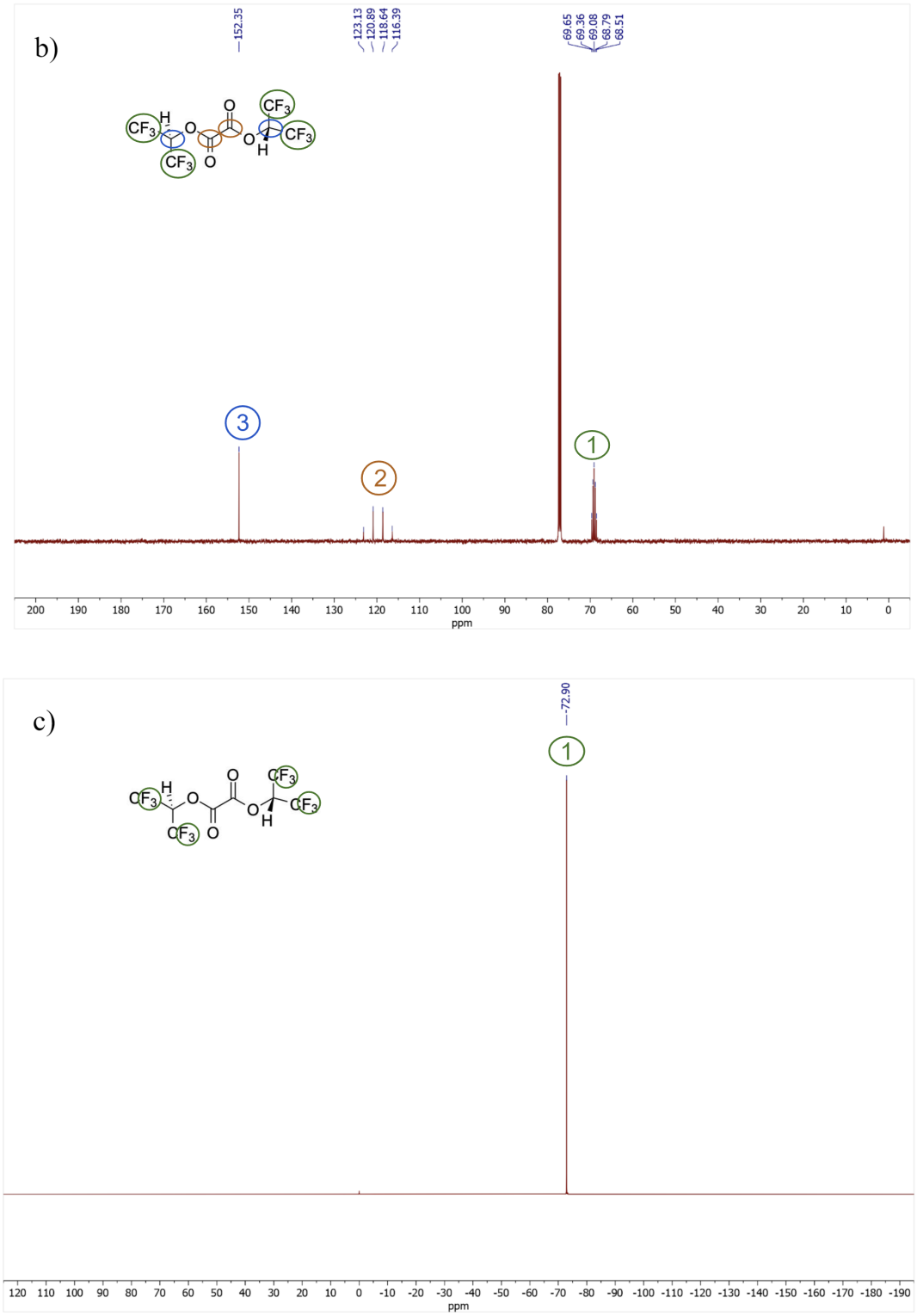


***Figure 4.2.2. Characterization of the FOC (bis(1,1,1,3,3,3-hexafluoropropan-2-yl) oxalate). a) $^{1}H$, b) $^{13}C$, c) $^{19}F$ NMR spectra.***

Moreover, synthesized FOC was soluble in the most common organic solvents like DCM, THF, and methanol which is advantageous for preparing various nanoplatforms.

### 4.3 Hydrogen Peroxide-Responsive Chemiluminescence of FOC-Rubrene System

Hydrogen peroxide-responsive chemiluminescence (CL) properties of FOC were examined in THF. 10 mg of FOC and 0.2 mg of rubrene were dissolved in THF. Upon the addition of 1 M hydrogen peroxide, a luminescence peak was observed at 560 nm (Figure 4.3.1). With time, the luminescence decreased substantially, indicating rapid perhydrolysis of FOC. Overall, the chemiluminescence spectra of the FOC-Rubrene were similar to the fluorescence spectra of the rubrene shown in Appendices 1.

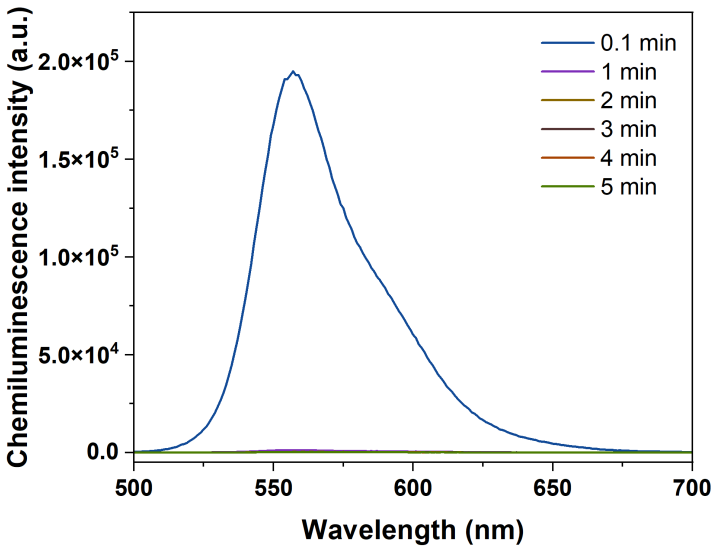


***Figure 4.3.1. Chemiluminescence profile of the FOC - Rubrene systems. Chemiluminescence spectra of 10 mg FOC and 0.2 mg Rubrene after the addition of 1 M $H_2O_2$ in THF. Measurement was conducted with a fluorescence spectrophotometer at 25 °C for 5 min.***

These results indicate that the reaction of the FOC with hydrogen peroxide may excite the fluorophore located nearby and exhibit chemiluminescence following the chemically initiated electron exchange luminescence (CIEEL) mechanism. In the presence of hydrogen peroxide, FOC can decompose to form 2 molecules 1,1,1,3,3,3-hexafluoro-2-propanol, that can generate distinct peaks in the $^{19}F$ NMR signal and unstable high energy intermediate 1,2-dioxetanedione that can excite fluorophore nearby. The intermediate gains an electron from the fluorophore and generates a fluorophore radical cation. The electron transfer processes are schematically summarized in Figure 4.3.2. Following back electron transfer from the anion to fluorophore cation results in the formation of fluorophore in the excited state. Therefore, chemiluminescence does not require an external source of excitation, which is beneficial in optical bioimaging through the suppression of autofluorescence. The rapid CL response of FOC showed the strong potential for the application of the compound to CL imaging of inflammatory diseases.

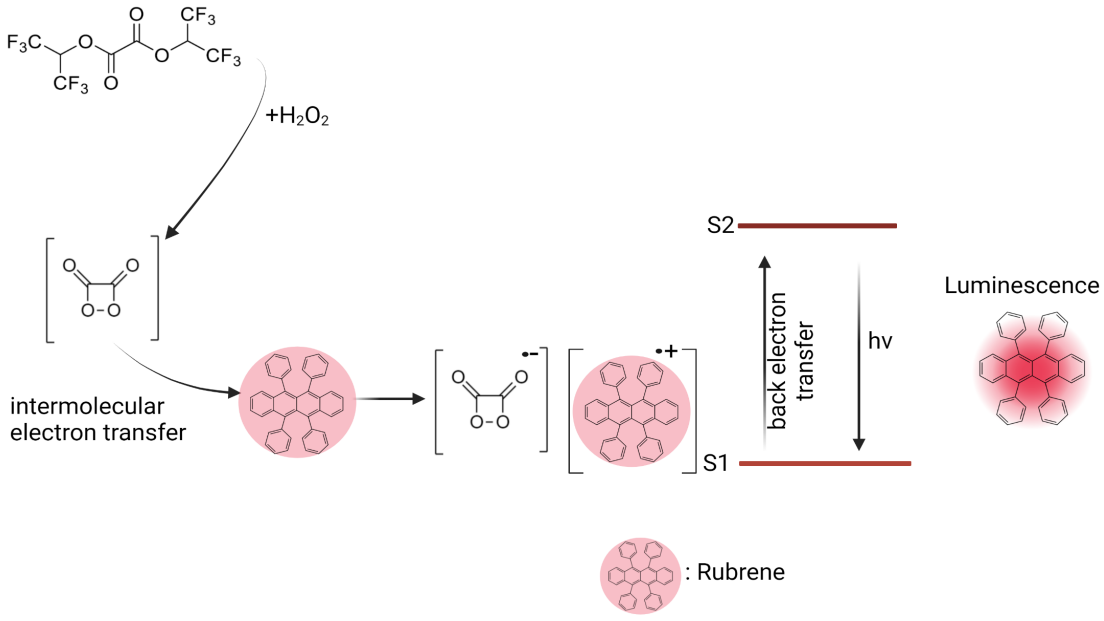


***Figure 4.3.2. Schematic illustration of the chemically initiated electron exchange luminescence (CIEEL) mechanism of the FOC - Rubrene system.***

### 4.4 Preparation and Characterization of Nanoparticles

FOC and dye systems were assembled into the nanoparticles. Pluronic F-127 was used as an amphiphilic polymer matrix endowing water dispersity and biocompatibility of the resulting nanoparticles, PLGA was used for the stability of the compounds, FOC as a $^{19}F$ MRI contrasting agent, CPPO was used as a chemical excitation source and dye as an energy acceptor and CL emitter. For the synthesis of the nanoparticles, an oil-in-water nanoemulsion solvent evaporation method was used. Also, a solvent drying and redispersion method was used. However, compared to the nanoemulsion solvent evaporation method, the resulting nanoparticles were larger in size and resulted in fewer FOC molecules (Appendices 2).

Formation of the nanoparticles occurred due to noncovalent interactions π–π stacking and hydrophobic forces resulting in the integration of fluorophore, FOC, and CPPO molecules in hydrophobic cores. Pluronic F-127 and PLGA molecules located at the interface stabilized the nanoparticles and located with the lipophilic components to the hydrophobic core and hydrophilic chains towards the water.

The average diameter of the obtained nanoparticles was around 20 nm, with narrow size distribution demonstrated by DLS results. The size was beneficial for systemic circulation *in vivo* applications. The transmission electron microscopy (TEM) image for nanoparticles is shown in Figure 4.4.1.(a). The particle sizes in DLS and TEM are well correlated.

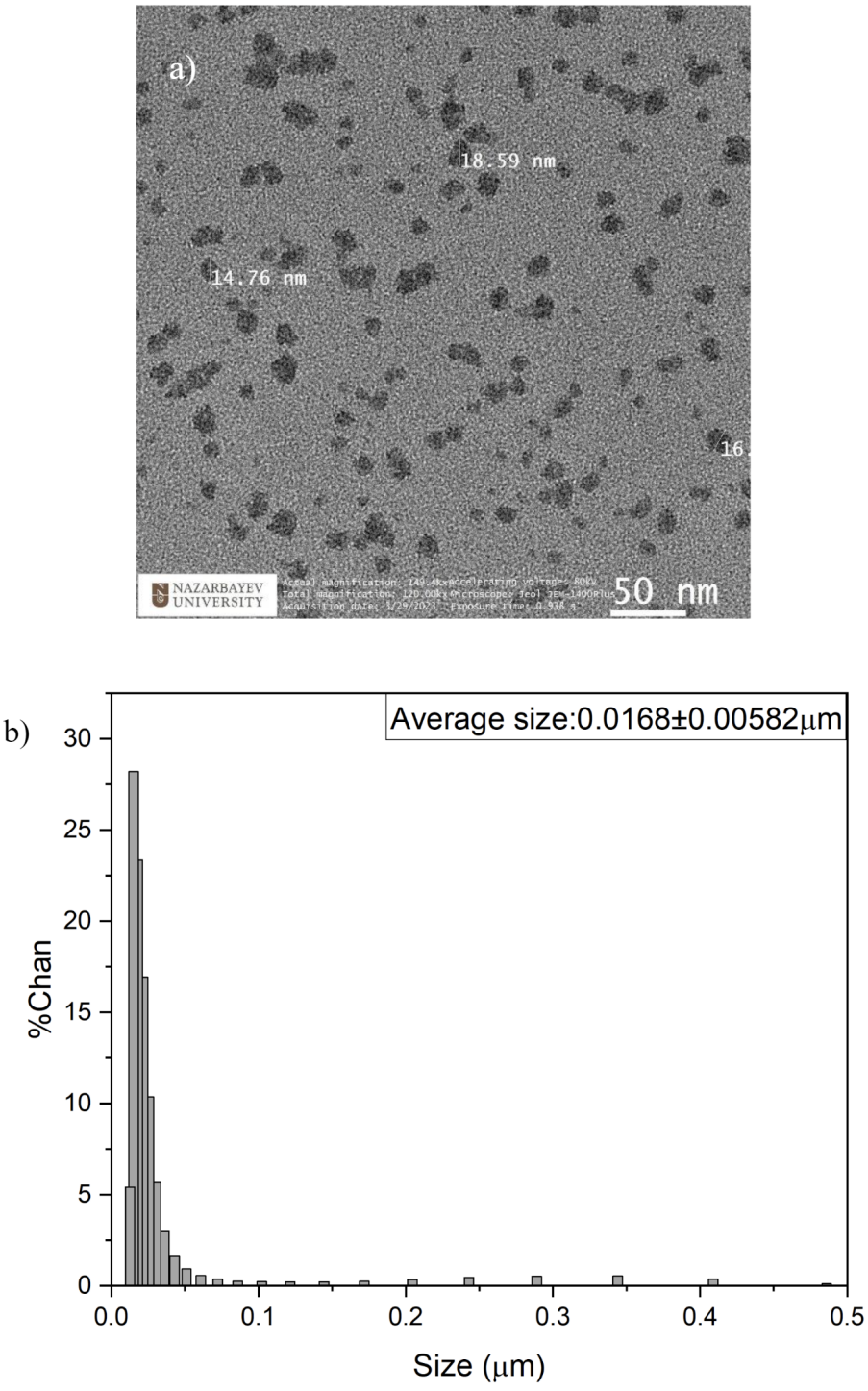


***Figure 4.4.1. Characterization of physicochemical properties of chemiluminescent nanoprobes. a) TEM images, b) Dynamic light scattering size distribution images.***

### 4.5 $^{19}$F NMR Spectra for the Nanoparticles

$^{19}$F NMR spectra of the FOC inside the nanoparticles were obtained, and the results indicate that more than 80% of FOC is preserved after 2 hours, as shown in Figure 4.5.1. Even there is a potential to be hydrolyzed in water, the nanoplatform prolongs the lifetime of FOC by stabilization in the hydrophobic matrix.

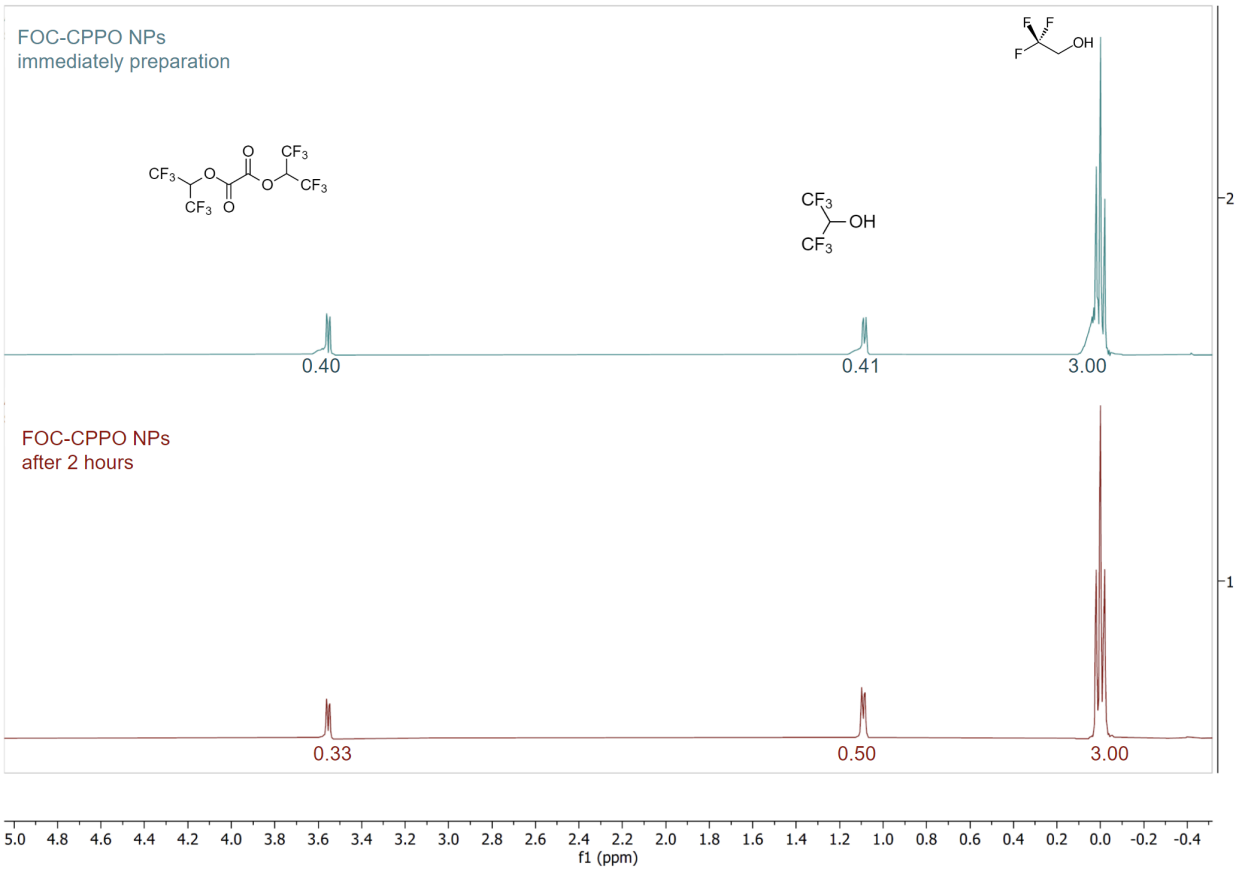


***Figure 4.5.1. $^{19}$F NMR spectra of FOC-CPPO nanoparticles taken immediately after preparation and 2 hours later.***

Hydrogen peroxide responsive behavior of the FOC in nanoparticles was studied in the $^{19}$F NMR spectra. Samples were measured immediately after the addition of hydrogen peroxide, which resulted in a decrease of FOC content by 22%. However, after 30 minutes, the FOC peak decreased

by 88.8%, as illustrated in Figure 4.5.2. After the addition of the hydrogen peroxide, the peak area corresponding to 1,1,1,3,3,3-hexafluoro-2-propanol was doubled.

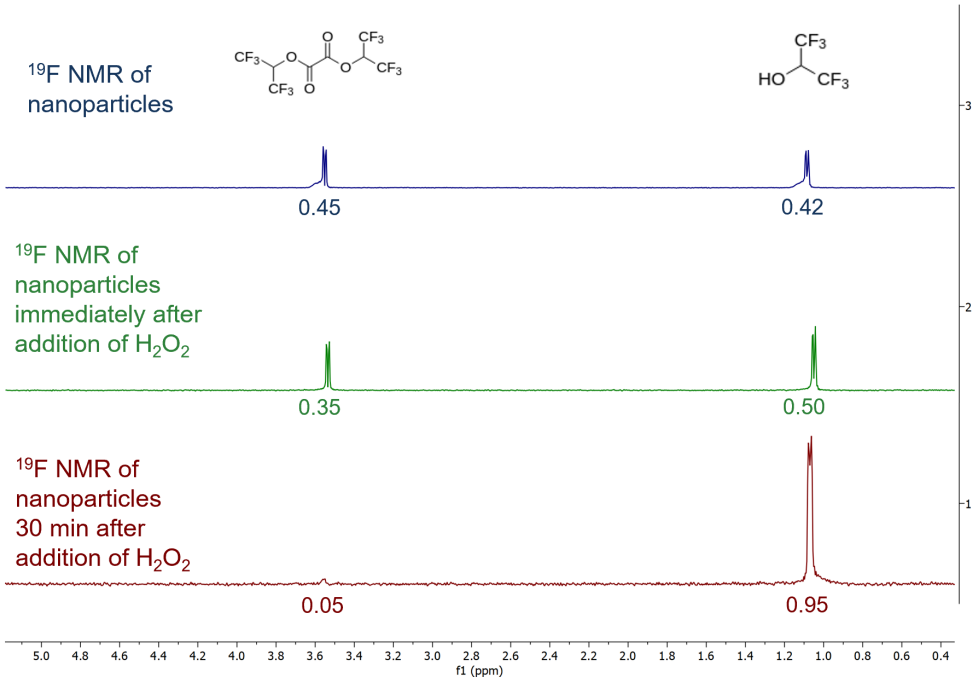


***Figure 4.5.2. $^{19}$F NMR spectra of FOC-CPPO nanoparticles, FOC-CPPO nanoparticles immediately after the addition of hydrogen peroxide, and FOC-CPPO nanoparticles 30 min after the addition of hydrogen peroxide.***

These results highlight the potential of FOC to act as a $^{19}$F MRI contrasting agent. Due to aggregation of the hydrophobic FOC molecules and the proximity of the fluorine atoms, $T_2$ relaxation time will be shortened, leading to suppressed $^{19}$F MRI signal. However, after the nucleophilic attack of the hydrogen peroxide on the FOC, the resulting hydrophilic fluorinated alcohol will be capable of prolonging $^{19}$F $T_2$ relaxation times due to the liberational motion of fluorinated segments. This hydrophobic to hydrophilic transition, accompanied by cleavage of the bonds, allows ratiometric imaging of the "turn-off" signal by FOC and the "turn-on" signal of 1,1,1,3,3,3-hexafluoro-2-propanol. As shown in Figure 4.5.3, the ratiometric imaging can provide

a 19-fold higher intensity after adding $H_2O_2$, showing the potential for strong contrast in ROS rich microenvironment.

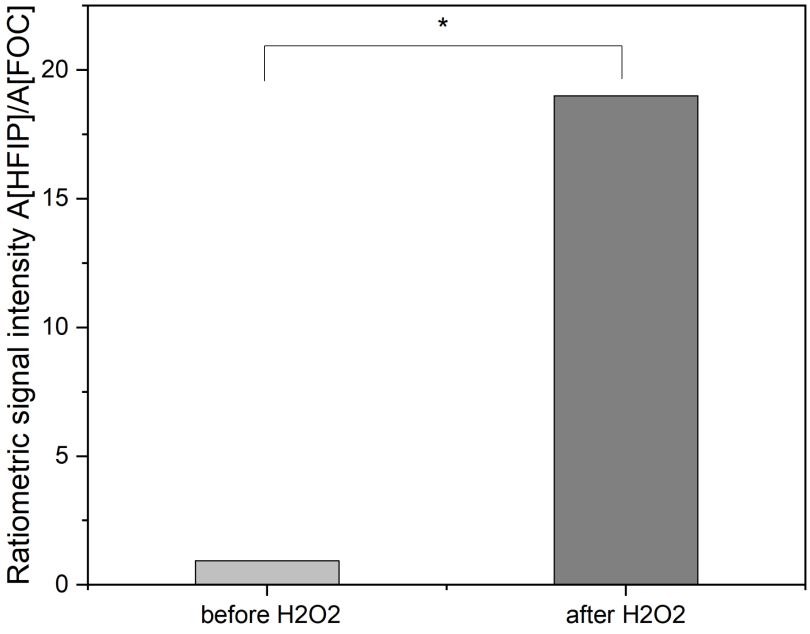


***Figure 4.5.3. The ratiometric signal intensity of $^{19}F$ NMR spectra of FOC-CPPO nanoparticles before and after the addition of hydrogen peroxide. Turn off and turn on signals for FOC and 1,1,1,3,3,3-hexafluoro-2-propanol.***

### 4.6 Chemiluminescence Spectra of the Nanoparticles

Chemiluminescence of the nanoparticles similar to the free dye was observed after adding the hydrogen peroxide. Notably, a persistent chemiluminescence signal was observed even after 50 minutes when the 1 M hydrogen peroxide was added. This prolonged sustained signal is advantageous for *in vivo* applications. Through the integration of the area under the curve, it was found that even within 0.1 min after the addition of hydrogen peroxide, around 560 times signal enhancement was achieved.

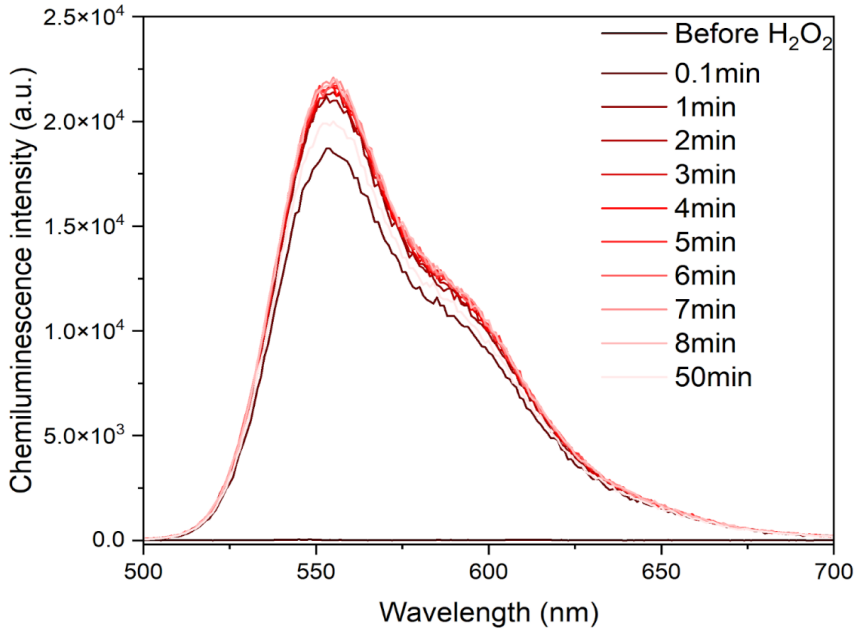


***Figure 4.6.1.1. Chemiluminescence spectra of the FOC-CPPO-Rubrene nanoparticles with time.***

The chemiluminescence intensity lasting several hours was achieved when hydrogen peroxide concentration was lowered to the physiologically relevant concentration of $10^{-5}$M (Figure 4.6.1.2). Thus, time-dependent chemiluminescent profiles depending on hydrogen peroxide concentration were observed. Prolonged chemiluminescence signal indicates that high energy intermediate 1,2-dioxetanedione was continuously produced and excitation of the rubrene dye was occurring. These patterns could be attributed to the slow perhydrolysis of the nanoparticles in the presence of the hydrogen peroxide and following gradual degradation of nanoparticles, with accompanying with a sustained release of drugs.

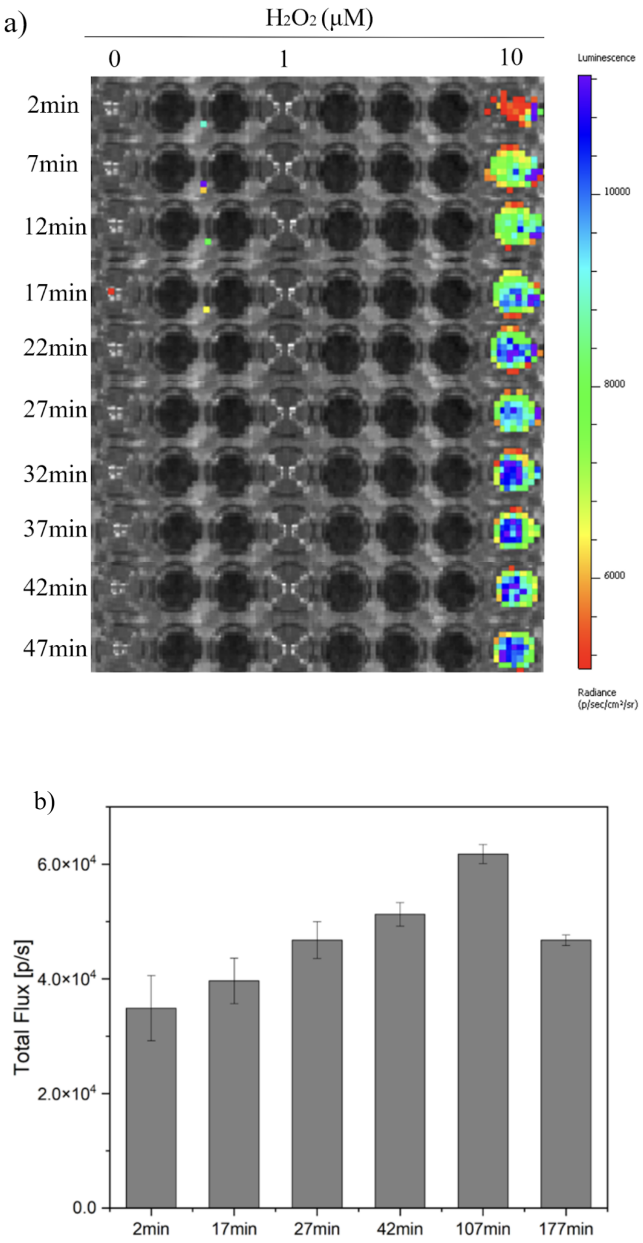


***Figure 4.6.1.2. Chemiluminescence of the nanoparticles at $10^{-5}$M hydrogen peroxide a) visualized and b) quantified using IVIS Spectrum CT.***

Degradation of the nanoparticles after the addition of the hydrogen peroxide was confirmed with the DLS measurements. As could be seen from Figure 4.4.1 and Figure 4.6.1.3, the average size of the nanoparticles was around 17 nm with a low error range. However, after adding

hydrogen peroxide, a small amount of the nanoparticles remained, and the majority of the nanoparticles were degraded and released the water-soluble contents. The free surfactant was randomly aggregated in the solution resulting in the broad distribution in the DLS and significantly large standard error (Figure 4.6.1.3).

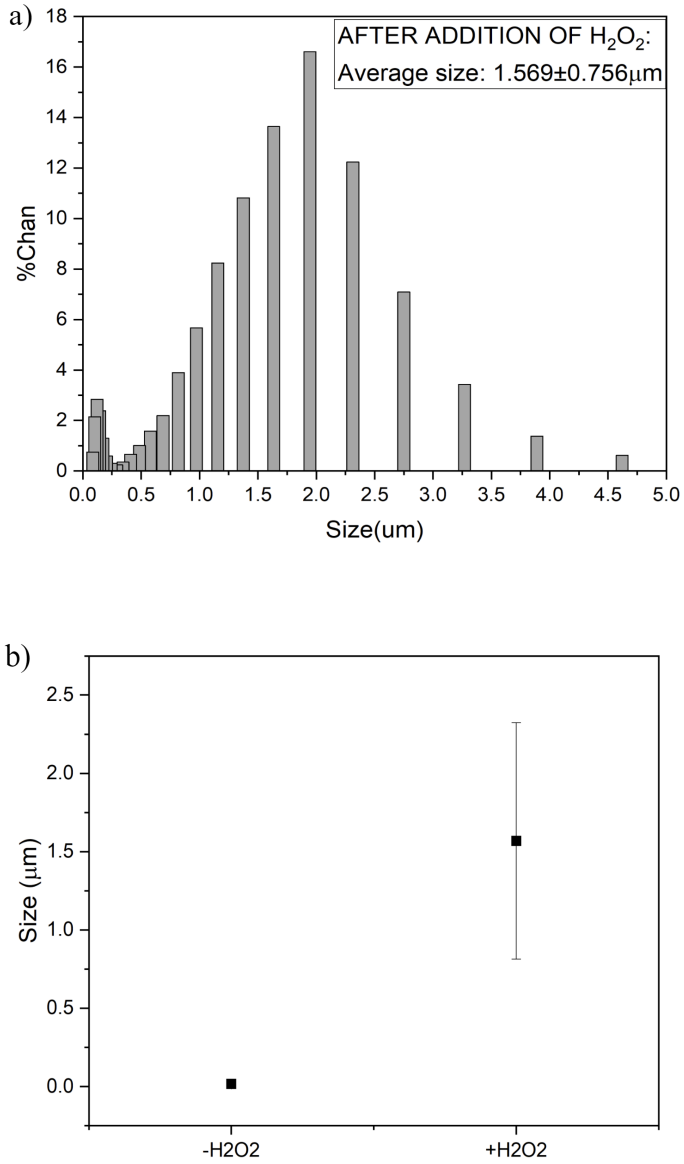


***Figure 4.6.1.3. Dynamic Light Scattering results a) after adding hydrogen peroxide b) average size ± standard error before and after adding hydrogen peroxide.***

### 4.7 Material Toxicity

Toxicity of the FOC-CPPO-rubrene nanoparticles were checked to determine the concentrations which would be biologically safe to use in *in vitro* systems. To identify the potential toxicity of the material 4 different concentrations were tested: 44 mg/ml, 22 mg/ml, 11mg/ml, 5.5 mg/ml. Additionally, positive and negative controls were included; the seeding scheme was provided in Table 3.6.1. The toxicity of the material was checked with an MTT assay.

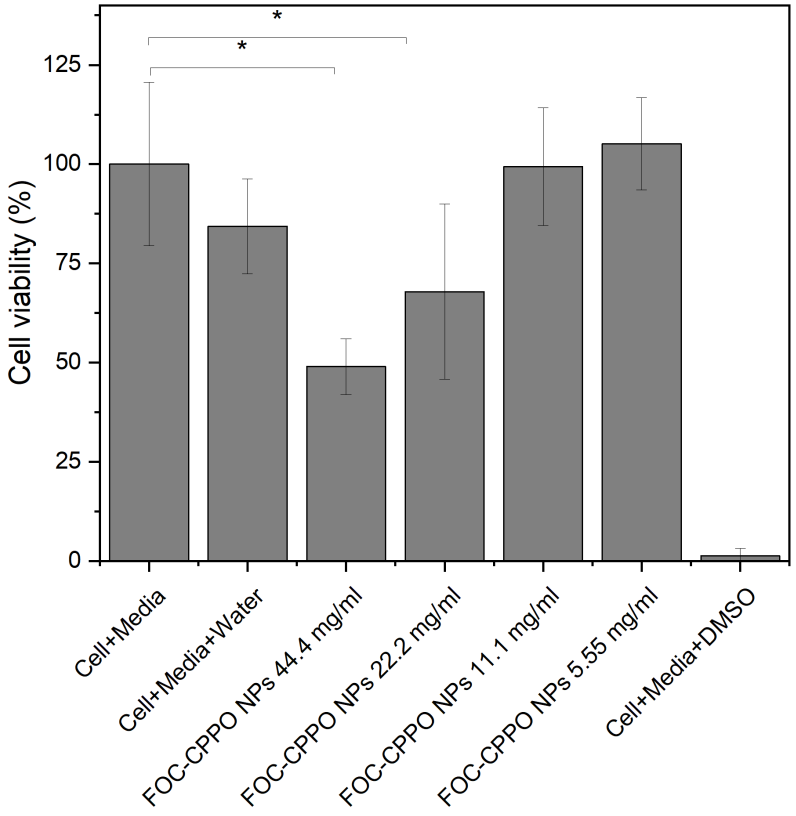


***Figure 4.7.1. Material toxicity test. The bars represent mean±standard deviation. Statistical significance was determined by ANOVA test, $p<0.05$.***

Overall, it is evident that FOC-CPPO nanoparticles exhibit cytotoxic activity in a dose-dependent manner. At the concentration of 44.4 mg/ml, the viability of the cells falls below 50%. However, at lower concentrations of nanoparticles 11.1 mg/ml, the toxicity of the material is almost negligible. Although FOC-CPPO nanoparticles showed the potential to cause cytotoxicity

on MRC-5 cell lines at higher concentrations, overall, preliminary results indicate that it is a biocompatible nanoplatform at the concentration of 11.1 mg/ml. Further material toxicity has to be checked on different cell strains.

### 4.8 ROS triggered drug release

To demonstrate ROS triggered therapeutic effect of FOC-CPPO nanoparticle, excess amounts of a photodynamic therapy (PDT) drug, Protoporphyrin IX (PpIX), that have a photoluminescence (PL), were loaded in the nanoparticle, and the intracellular PL intensity was compared at ROS rich and normal microenvironments. Although increasing the luminophore (LP) content may result in an increase in the PL intensity, an excessive amount of the LP results in concentration quenching. An intracellular release of LPs from LP excess-loaded nanoparticles in a certain condition may turn on the PL, which can be detected by the fluorescence cell imaging method. Increasing the amount of the PpIX loaded into the nanoparticle up to 50 times resulted in an abrupt decrease in the PL, but the CL was maximum at the highest amount (Figure 4.8.1.). The efficiency of the CL was correlated with the perhydrolysis reactivity and the efficiency of the energy transfer from high energy chemical intermediate. Therefore, CL quantum yields were not directly correlated with PL quantum yields, chemiluminescence's localized reaction and excitation feature. Since we need highly PL quenched nanoparticles for the therapy (drug release) experiment, we selected the 50 times higher PpIX-loaded nanoparticle to observe an enhanced intracellular PL intensity depending on ROS concentration.

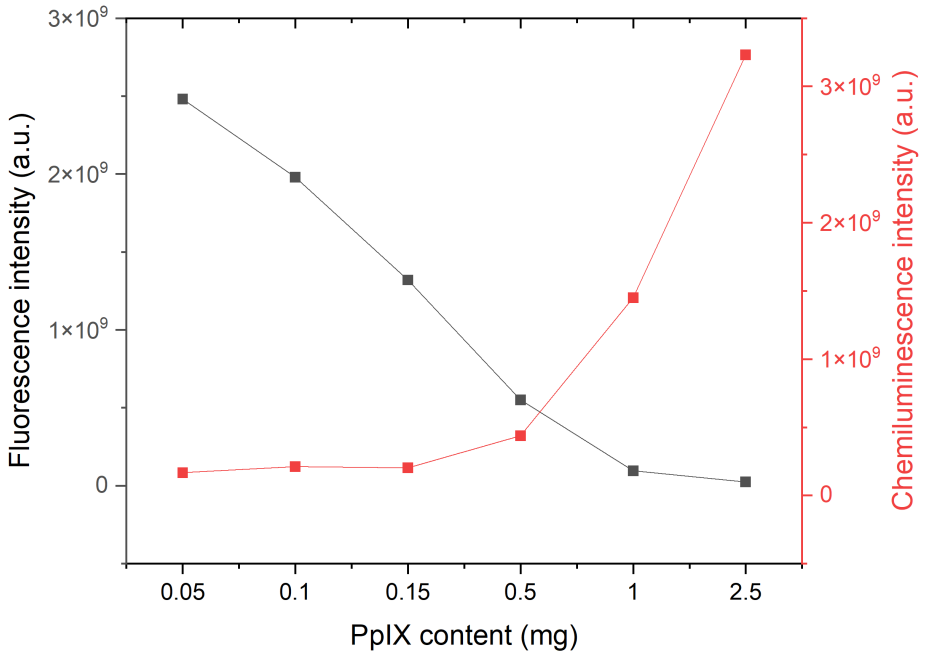


***Figure 4.8.1. PpIX concentration dependent photoluminescence and chemiluminescence intensity of nanoparticles.***

Oxidative stress in the cells is associated with the generation of intracellular reactive oxygen species. The oxidative stress was simulated by inducing hypoxia through overnight incubation of the cells in hypoxic (anaerobic) conditions. The internalization and drug release profiles of the FOC-CPPO-PpIX nanoparticles were studied. The nanoparticles containing up to 2.5mg of PpIX dye were used in this experiment to reach the PL concentration quenching. Time-dependent cellular uptake and subsequent drug release were studied by fluorescence microscopy. Overall, higher fluorescence intensity was observed in hypoxic conditions (Figure 4.8.2.(a)). This could be attributed to the higher oxidative stress and higher ROS contents in the cells in hypoxia. Interaction of the nanoparticles with the intracellular ROS triggers perhydrolysis of the FOC and CPPO in the hydrophobic core of the nanoparticles. This may trigger the release of the photosensitizer drug and, therefore, higher fluorescent signal intensity. Incubation time of 24 hours

results in quite a high cytotoxicity of the material due to the photosensitizing ability of PpIX and the generation of toxic singlet oxygen. Moreover, due to the fact that hypoxic conditions develop within 12 hours, the cells incubated for 24 hours were shown to be most susceptible to the treatment. The incubation time of 12 hours has shown the highest PL intensity because of the efficient internalization and expression of the dye. Shorter incubation times showed slightly lower signal intensity which could be attributed to the ongoing perhydrolysis of the nanoparticles and drug release. Imaging of the FOC-CPPO nanoparticles loaded with PpIX inside the cells showed accumulation in close proximity to the mitochondria. This could be attributed to the fact that mitochondria are the intracellular source of ROS [34]. Due to the concentration quenching of the PpIX inside of the nanoparticles, time-dependent degradation of the nanoparticles results in the release of free PpIX and, thus, increased fluorescence intensity.

a)

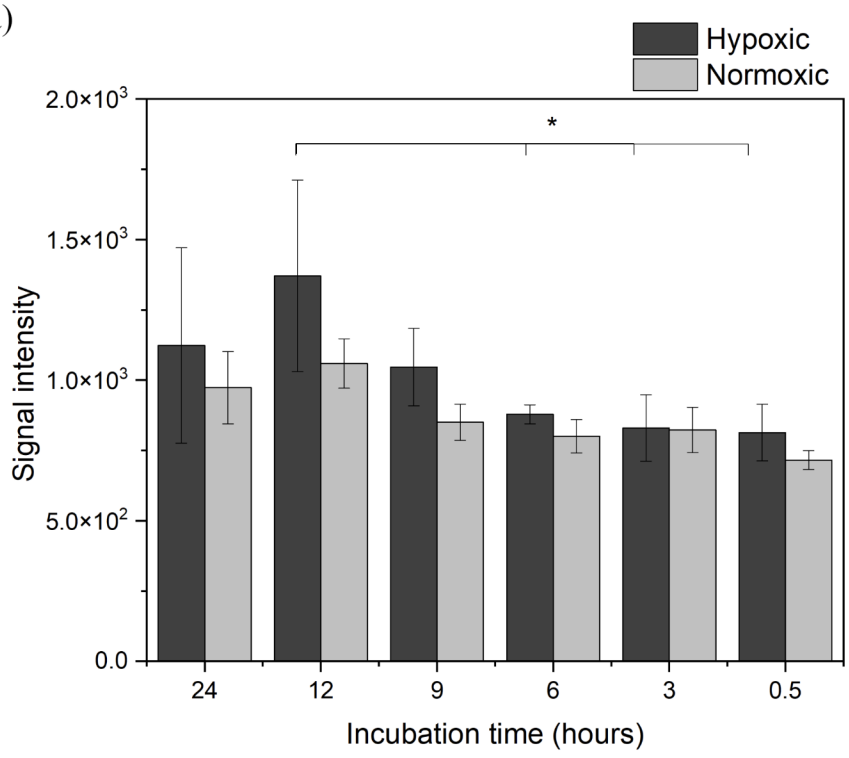

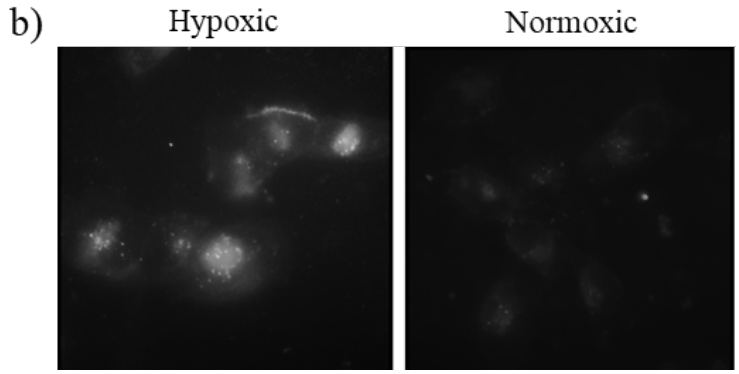


***Figure 4.8.2. ROS triggered PpIX drug release from FOC-CPPO nanoparticles b) fluorescent cell images at 9 hours incubation.***

# Chapter 5 - Conclusion

In summary, a theranostic system, which can image (diagnose) as well as release drugs (therapy) in a specific biomarker-rich environment, is a hot topic in biomedical research. Herein, fluorinated oxalate compound was synthesized and the reactivity towards reaction with hydrogen peroxide was estimated with DFT calculations. Then, a hydrogen peroxide responsive biocompatible chemiluminescent nanoplatform with tunable emission wavelength accompanied by a “turn on” 19F MRI signal and hydrophobic drugs release was developed. The nanoparticle exhibited 560-fold chemiluminescence signal enhancement in the reaction with hydrogen peroxide. Chemiluminescence intensity and emission wavelength could be tuned by varying the fluorophores. It was found that polycyclic aromatic compounds with low oxidation potential exhibit high chemiluminescence quantum yield in the POCL reaction. Moreover, the physiologically relevant concentration of hydrogen peroxide could be visualized. Radiometric imaging of $^{19}F$ NMR was also realized with 19-fold signal enhancement. The hydrogen peroxide concentration-dependent drug release profile of the nanoparticle was confirmed by tracking the

fluorescence of PDT drug in hypoxia-induced MRC5 cells. Thus, developed nanoparticle holds the potential for imaging of diseases associated with high ROS levels, such as inflammations or cancer accompanied by drug delivery. Further optimizations are required to reveal the US potential of the nanoparticles. The findings of this study provide a versatile platform for further research with broad implications.

# Bibliography

[1] M. C. Boonstra, S. W. L. De Geus, H. A. J. M. Prevoo, L. J. A. C. Hawinkels, C. J. H. Van De Velde, P. J. K. Kuppen, A. L. Vahrmeijer, and C. F. M. Sier, "Selecting targets for tumor imaging: An overview of cancer-associated membrane proteins," *Biomarkers in Cancer*, vol. 8, 2016.

[2] R. H. Fang, W. Gao, and L. Zhang, "Targeting drugs to tumours using cell membrane-coated nanoparticles," *Nature Reviews Clinical Oncology*, vol. 20, no. 1, pp. 33–48, 2022.

[3] S. T. Barry, D. I. Gabrilovich, O. J. Sansom, A. D. Campbell, and J. P. Morton, "Therapeutic targeting of tumour myeloid cells," *Nature Reviews Cancer*, vol. 23, no. 4, pp. 216–237, 2023.

[4] W. Yi, P. Xiao, X. Liu, Z. Zhao, X. Sun, J. Wang, L. Zhou, G. Wang, H. Cao, D. Wang, and Y. Li, "Recent advances in developing active targeting and multi-functional drug delivery systems via bioorthogonal chemistry," *Signal Transduction and Targeted Therapy*, vol. 7, no. 1, 2022.

[5] H. Sies, V. V. Belousov, N. S. Chandel, M. J. Davies, D. P. Jones, G. E. Mann, M. P. Murphy, M. Yamamoto, and C. Winterbourn, "Defining roles of specific reactive oxygen species (ROS) in cell biology and physiology," *Nature Reviews Molecular Cell Biology*, vol. 23, no. 7, pp. 499–515, 2022.

[6] E. R. Brannon, M. V. Guevara, N. J. Pacifici, J. K. Lee, J. S. Lewis, and O. Eniola-Adefeso, "Polymeric particle-based therapies for acute inflammatory diseases," *Nature Reviews Materials*, vol. 7, no. 10, pp. 796–813, 2022.

[7] Z. Tu, Y. Zhong, H. Hu, D. Shao, R. Haag, M. Schirner, J. Lee, B. Sullenger, and K. W. Leong, "Design of therapeutic biomaterials to control inflammation," *Nature Reviews Materials*, vol. 7, no. 7, pp. 557–574, 2022.

[8] A. M. Garcia-Campana and W. R. G. Baeyens, "Mechanism and Application of Peroxyoxalate Chemiluminescence," in *Chemiluminescence in Analytical Chemistry*, New York: Marcel Dekker, Inc, 2001.

[9] A. Boaro and F. H. Bartoloni, "Peroxyoxalate high-energy intermediate is efficiently decomposed by the catalyst imidazole," *Photochemistry and Photobiology*, vol. 92, no. 4, pp. 546–551, 2016.

[10] E. C. Cheung and K. H. Vousden, "The role of ROS in tumour development and progression," *Nature Reviews Cancer*, vol. 22, no. 5, pp. 280–297, 2022.

[11] C. Andreou, R. Weissleder, and M. F. Kircher, "Multiplexed imaging in oncology," Nature Biomedical Engineering, vol. 6, no. 5, pp. 527–540, 2022.

[12] G. Saravanakumar, J. Kim, and W. J. Kim, "Reactive-oxygen-species-responsive drug delivery systems: Promises and challenges," *Advanced Science*, vol. 4, no. 1, p. 1600124, 2016.

[13] Y. Yang and F. Zhang, "Activatable chemiluminescent molecular probes for Bioimaging and Biosensing," *Analysis & Sensing*, vol. 1, no. 2, pp. 75–89, 2021.

[14] P. Cheng and K. Pu, "Molecular imaging and disease theranostics with renal-clearable optical agents," *Nature Reviews Materials*, vol. 6, no. 12, pp. 1095–1113, 2021.

[15] Y. Yang and F. Zhang, "Activatable chemiluminescent molecular probes for Bioimaging and Biosensing," *Analysis & Sensing*, vol. 1, no. 2, pp. 75–89, 2021.

[16] J. B. Grimm and L. D. Lavis, "Caveat fluorophore: An insiders' guide to small-molecule fluorescent labels," *Nature Methods*, vol. 19, no. 2, pp. 149–158, 2021.

[17] Z. Wang, J. Huang, J. Huang, B. Yu, K. Pu, and F. J. Xu, "Chemiluminescence: From mechanism to applications in biological imaging and therapy," *Aggregate*, vol. 2, no. 6, 2021.

[18] J. Huang and K. Pu, "Activatable molecular probes for second near-infrared fluorescence, chemiluminescence, and photoacoustic imaging" *Angewandte Chemie*, vol. 132, no. 29, pp. 11813–11827, 2020.

[19] J. Huang, J. Li, Y. Lyu, Q. Miao, and K. Pu, "Molecular optical imaging probes for early diagnosis of drug-induced acute kidney injury," *Nature Materials*, vol. 18, no. 10, pp. 1133–1143, 2019.

[20] D. Cui, J. Li, X. Zhao, K. Pu, and R. Zhang, "Semiconducting polymer nanoreporters for near-infrared chemiluminescence imaging of immunoactivation," Advanced Materials, vol. 32, no. 6, p. 1906314, 2019.

[21] S. Ye, N. Hananya, O. Green, H. Chen, A. Q. Zhao, J. Shen, D. Shabat, and D. Yang, "A highly selective and sensitive chemiluminescent probe for real-time monitoring of hydrogen peroxide in cells and animals," *Angewandte Chemie International Edition*, vol. 59, no. 34, pp. 14326–14330, 2020.

[22] J. Chen, L. Chen, Y. Wu, Y. Fang, F. Zeng, S. Wu, and Y. Zhao, "A H2O2-activatable nanoprobe for diagnosing interstitial cystitis and liver ischemia-reperfusion injury via multispectral optoacoustic tomography and NIR-II Fluorescent Imaging," *Nature Communications*, vol. 12, no. 1, 2021.

[23] P. Sun, F. Qu, C. Zhang, P. Cheng, X. Li, Q. Shen, D. Li, and Q. Fan, "Nir-II excitation Phototheranostic platform for synergistic photothermal therapy/chemotherapy/chemodynamic therapy of breast cancer bone metastases," *Advanced Science*, vol. 9, no. 33, p. 2204718, 2022.

[24] X. Yan, W. Lin, H. Liu, W. Pu, J. Li, P. Wu, J. Ding, G. Luo, and J. Zhang, "Wavelength-tunable, long lifetime, and biocompatible luminescent nanoparticles based on a vitamin e-derived material for inflammation and tumor imaging," *Small*, vol. 17, no. 25, p. 2100045, 2021.

[25] J. Jeon, D. G. You, W. Um, J. Lee, C. H. Kim, S. Shin, S. Kwon, and J. H. Park, "Chemiluminescence resonance energy transfer–based nanoparticles for quantum yield–enhanced cancer phototheranostics," *Science Advances*, vol. 6, no. 21, 2020.

[26] J. Jeon, B. Yoon, S. H. Song, W. Um, Y. Song, J. Lee, D. G. You, J. Y. An, and J. H. Park, "Chemiluminescence resonance energy transfer-based immunostimulatory nanoparticles for sonoimmunotherapy," *Biomaterials*, vol. 283, p. 121466, 2022.

[27] J. Ding, G. Lu, W. Nie, L. L. Huang, Y. Zhang, W. Fan, G. Wu, H. Liu, and H. Y. Xie, "Self-activatable photo-extracellular vesicle for synergistic trimodal anticancer therapy," *Advanced Materials*, vol. 33, no. 7, p. 2005562, 2021.

[28] Y. C. Chen, Y. J. Liu, C. L. Lee, K. Y. Pham, D. Manoharan, S. Thangudu, C. H. Su, and C. S. Yeh, "Engineering $H_2O_2$ and $O_2$ self-supplying nanoreactor to conduct synergistic chemiexcited photodynamic and calcium-overloaded therapy in orthotopic hepatic tumors," *Advanced Healthcare Materials*, vol. 11, no. 20, 2022.

[29] L. Wu, Y. Ishigaki, W. Zeng, T. Harimoto, B. Yin, Y. Chen, S. Liao, Y. Liu, Y. Sun, X. Zhang, Y. Liu, Y. Liang, P. Sun, T. Suzuki, G. Song, Q. Fan, and D. Ye, "Generation of hydroxyl radical-activatable ratiometric near-infrared bimodal probes for early monitoring of tumor response to therapy," *Nature Communications*, vol. 12, no. 1, 2021.

[30] L. Su, Y. Chen, H. Huo, N. Liao, Y. Wu, X. Ge, Z. Guo, Z. Chen, X. Zhang, and J. Song, "Nir-II ratiometric chemiluminescent/fluorescent reporters for real-time monitoring and evaluating cancer photodynamic therapy efficacy," *Small*, vol. 18, no. 41, p. 2202551, 2022.

[31] D. Taherinia and A. Fattahi, "Inducing high exo selectivity in Diels–Alder reaction by Dimethylborane Substituent: A DFT study," *Scientific Reports*, vol. 12, no. 1, 2022.

[32] R. LeSar, Introduction to computational materials science: Fundamentals to applications. Cambridge: Cambridge University Press, 2016.

[33] Gaussian 16, Revision C.01, J. Frisch, W. Trucks, B. Schlegel, E. Scuseria, Gaussian, Inc., Wallingford CT, 2016.

[34] Y.-H. Lin, H.-M. Chang, F.-P. Chang, C.-R. Shen, C.-L. Liu, W.-Y. Mao, C.-C. Lin, H.-S. Lee, and C.-N. Shen, "Protoporphyrin IX accumulation disrupts mitochondrial dynamics and function in ABCG2-deficient hepatocytes," *FEBS Letters*, vol. 587, no. 19, pp. 3202–3209, 2013.

# Appendices

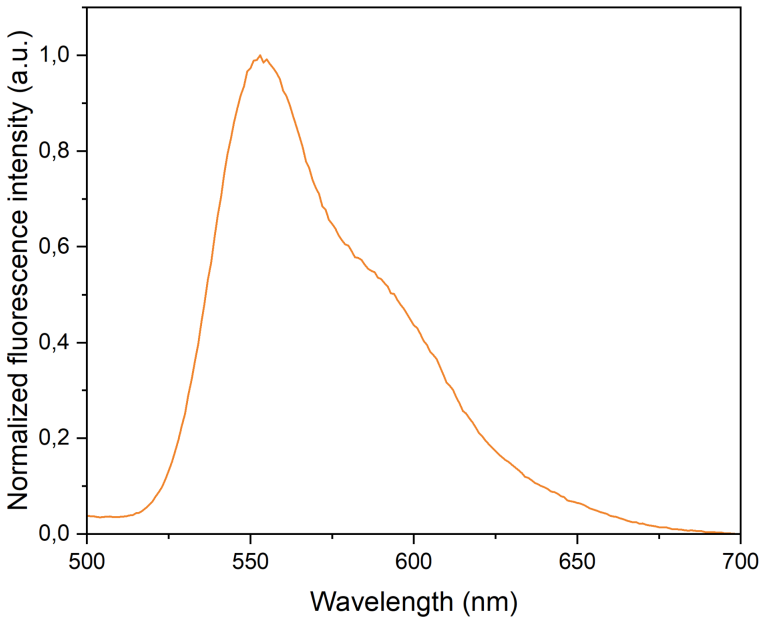


**Appendices 1. Normalized Fluorescence of Rubrene in THF**

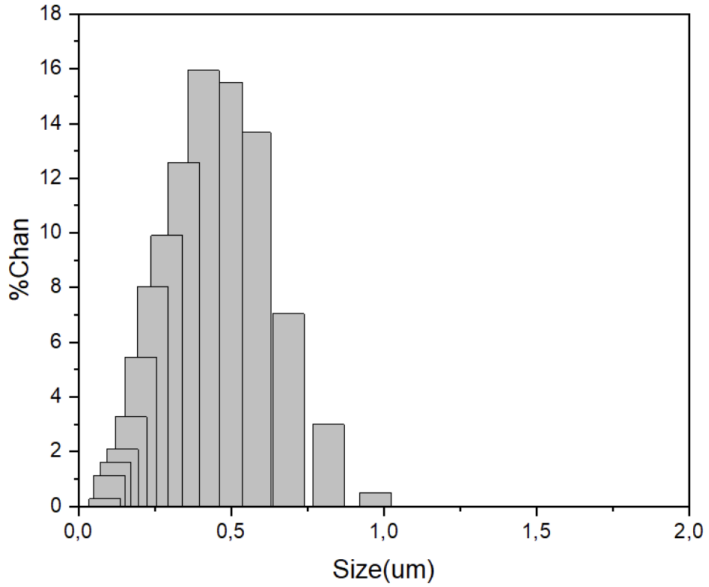


**Appendices 2. DLS of the nanoparticles prepared with solvent drying method.**

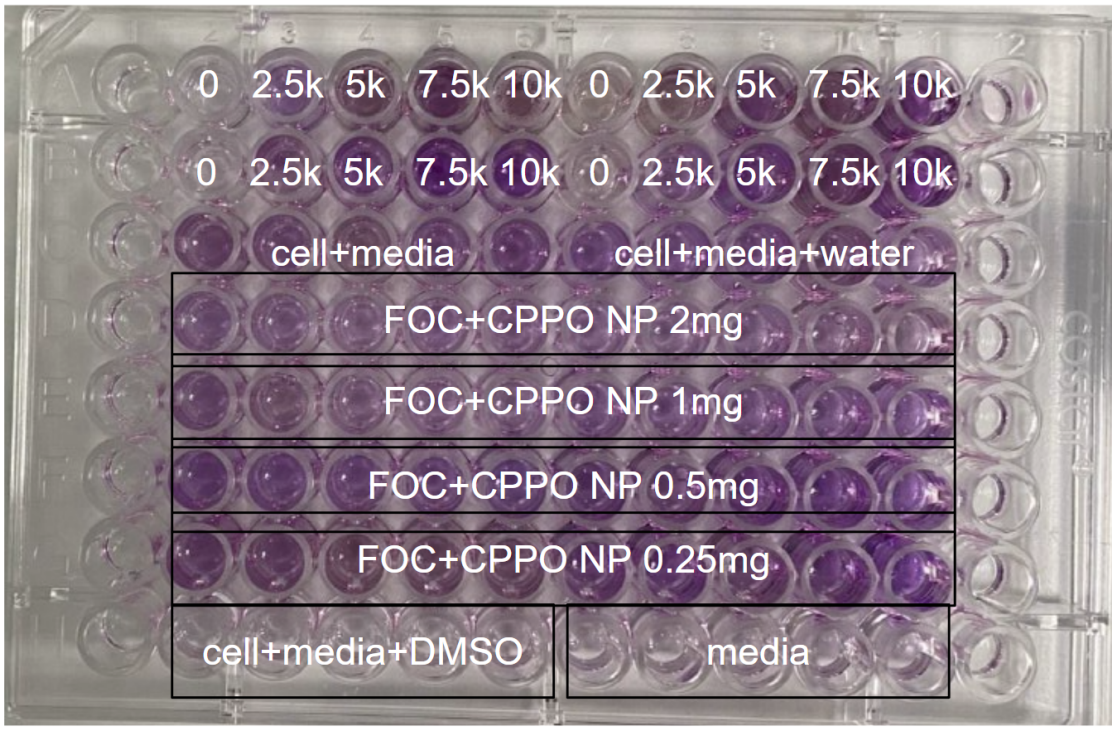


**Appendices 3. The 96-well plate with the cell seeding scheme for cell viability assay.**

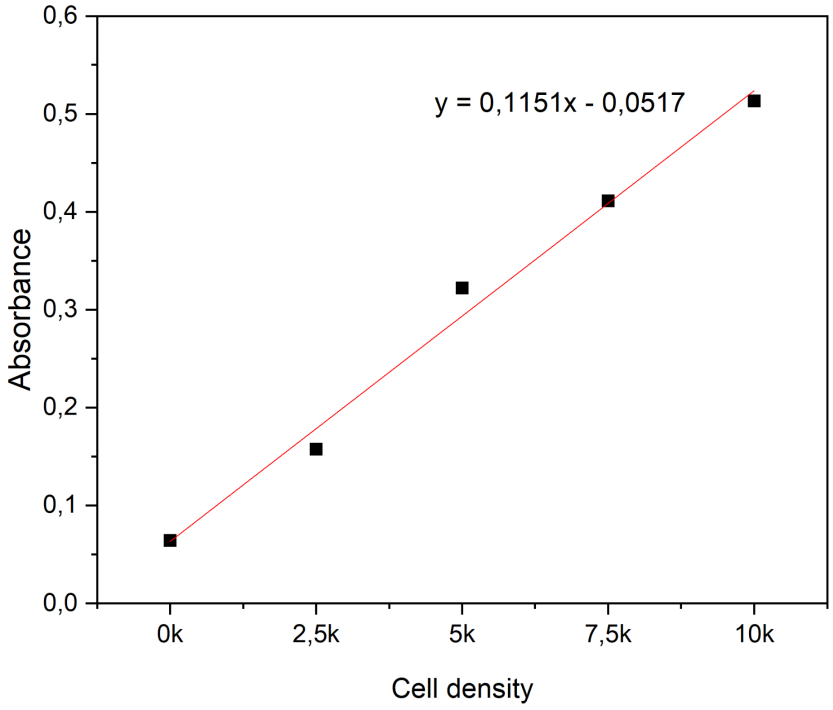


**Appendices 4. Standard curve for cell viability assay.**

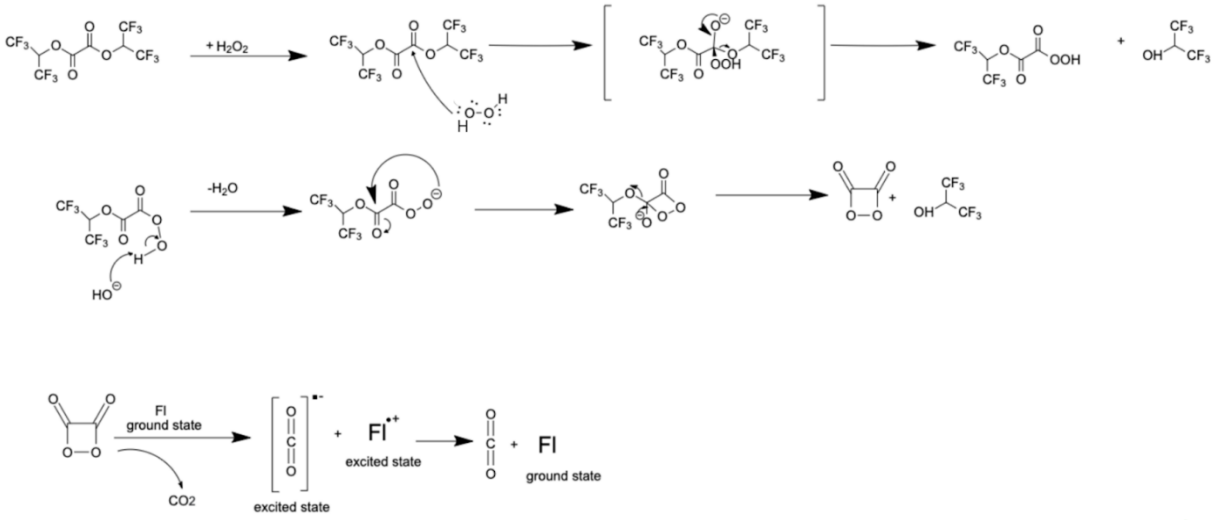


**Appendices 5. Mechanism for perhydrolysis reaction.**

**Appendices 6. Table of optimized geometries and calculated energies.**

| | | | |
|---|---|---|---|
| 1 | 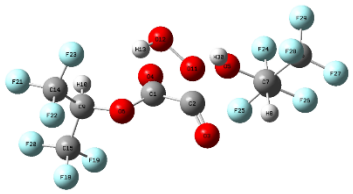 | optimized TS for the FOC+$H_2O_2$ | E=-1955.085921 Hartree |
| 2 | 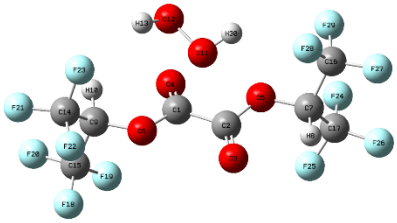 | reaction with hydrogen peroxide: reactant state | E=-1955.150841 Hartree |
| 3 | 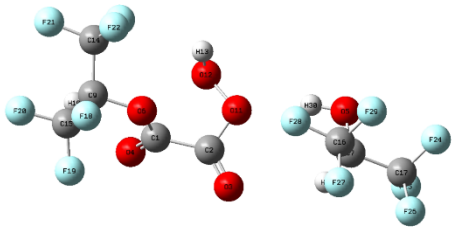 | reaction with hydrogen peroxide IM1 | E=-1955.143593 Hartree |

| | | | |
|---|---|---|---|
| 4 | 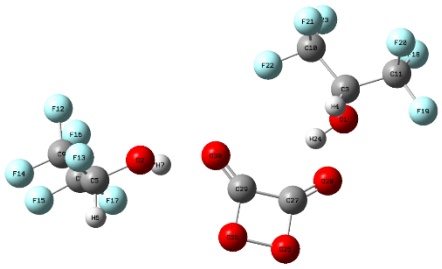 | reaction with hydrogen peroxide HEI product | E= -1954.9679926Hartree |
| 5 | 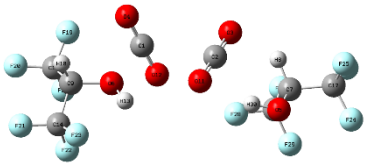 | reaction with hydrogen peroxide final product | E=1954.987674 Hartree |
| 6 | 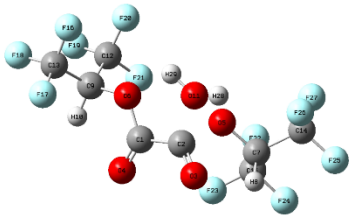 | TS optimized for the FOC+H2O | E=-1880.025943 Hartree |
| 7 | 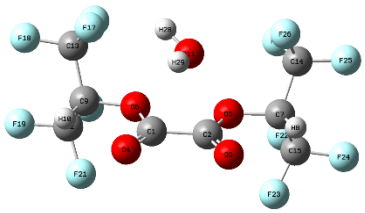 | reaction with water reactant state | E=-1880.087327 Hartree |
| 8 | 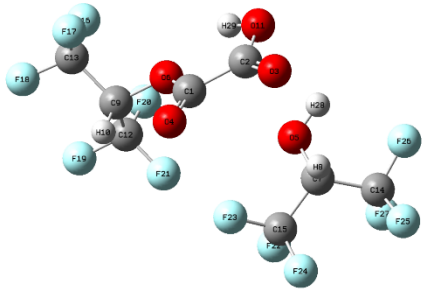 | reaction with water product state | E=-1880.091982 Hartree |